Nano Research

Open Access

Research Article

Unveiling the mechanism of selective CO_2 hydrogenation to CO on amorphous black TiO_X in thermal and photo-assisted thermal catalysis: The role of defects in amorphous structure and light irradiation

Mohammad Fereidooni[1,§], Mohammad Yazdanpanah[1,§], Victor Márquez[1], C. V. Paz[1], Martin Salazar Villanueva[2], Supareak Praserthdam[1,3], and Piyasan Praserthdam[1] ✉

[1] *Center of Excellence on Catalysis and Catalytic Reaction Engineering, Department of Chemical Engineering, Faculty of Engineering, Chulalongkorn University, Bangkok 10330, Thailand*
[2] *Facultad de Ingeniería, Benemerita Universidad Autonoma de Puebla, Apartado Postal J-39, CP 72570 Puebla, Mexico*
[3] *High-Performance Computing Unit (CECC-HCU), Department of Chemical Engineering, Faculty of Engineering, Chulalongkorn University, Bangkok 10330, Thailand*
[§] *Mohammad Fereidooni and Mohammad Yazdanpanah contributed equally to this work.*

Cite this article: *Nano Research*, **2025**, *18*, 94907218. https://doi.org/10.26599/NR.2025.94907218

ABSTRACT: Developing catalysts capable of efficiently utilizing both visible and near-infrared wavelengths of the solar spectrum for CO_2 hydrogenation has led to growing interest in reduced TiO_2 materials. Achieving efficient long-wavelength solar light harvesting requires a high concentration of oxygen vacancies (O_V). However, extensive O_V formation can lead to atomic rearrangements within TiO_X, causing a dispersion of O_V throughout the material, as opposed to creating localized and distinct O_V sites typical of crystalline TiO_X, which interact directly with reactants. In this study, we synthesized amorphous black TiO_X (AM-TiO_X) catalysts and thoroughly characterized their surface properties, including acidity and the desorption bond strengths of H_2 and CO_2. Density functional theory (DFT) simulations were performed to analyze the hydrogen adsorption profile and structural changes in the material due to O_V formation. We found that hydrogen mobility on the surface is restricted due to strong hydrogen bonding. The CO_2 hydrogenation process was investigated using *in situ* diffuse reflectance infrared Fourier transform spectroscopy (DRIFTS), enabling the development of a reaction pathway to elucidate the catalyst's selectivity towards CO and the effect of light irradiation on product formation rates. Notably, m-HCO_3* formation was favored, with CO and CH_4 production proceeding primarily via the formate pathway. To enhance catalyst stability against oxidation during reaction, the surface was decorated with Ru particles. The findings of this study are relevant to catalysts that leverage extensive O_V formation as a strategy to extend light responsiveness, as well as to the design of catalysts for CO_2 hydrogenation to CO.

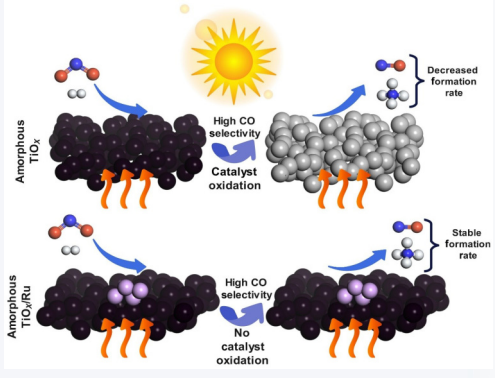

KEYWORDS: oxygen vacancy, amorphous, catalytic CO_2 hydrogenation, hydrogen mobility, photo-thermal, reaction mechanism analysis

1 Introduction

Carbon dioxide is a major contributor to global warming, with its massive emissions from fossil fuel consumption leading to significant environmental consequences [1, 2]. However, CO_2 also presents an opportunity as a valuable carbon source that can be harnessed not only to produce commodity chemicals but also for advancing sustainable technologies [3, 4]. In recent years, various sustainable approaches for CO_2 hydrogenation and reduction have been extensively studied, yielding promising results [5–7]. Among these approaches, photo-assisted thermal catalysis and photothermal catalysis stand out for their unique advantage of utilizing solar energy to generate electron-hole pairs [8, 9]. In these processes, the formation of charge carriers reduces the activation

Received: November 3, 2024; **Revised:** December 1, 2024
Accepted: December 25, 2024

✉Address correspondence to piyasan.p@chula.ac.th

energy barrier of the catalyst, thereby enhancing the reaction rate at lower temperatures [10, 11]. A recent strategy to optimize semiconductor catalysts for visible and near-infrared (NIR) light absorption, enhancing solar energy harvesting for both temperature increase and electron-hole pair generation, involves the creation of oxygen vacancies (O_V) [12, 13].

Reduced TiO_2, commonly known as black TiO_2, has recently gained significant attention for its potential in photocatalytic CO_2 reduction and hydrogen evolution [14–16]. The introduction of O_V in TiO_2 extends its light absorption to longer wavelengths, including the visible and NIR regions, addressing a major limitation of this material in solar-driven photocatalysis [17]. To efficiently harvest solar light-particularly in the NIR region, a high level of O_V formation in TiO_2 is necessary. However, this modification also intensifies charge carrier recombination, leading to a substantial decrease in photocatalytic activity [18]. Additionally, the band edge shifts associated with O_V creation result in a lower redox potential [19], further diminishing the material's photocatalytic efficiency for oxidation reactions. To overcome these challenges, photocatalytic CO_2 reduction and hydrogen evolution on black TiO_2 are often facilitated by the addition of sacrificial reagents such as methanol or triethanolamine, and by decorating the catalyst with noble metals like platinum [20]. However, the use of sacrificial reagents introduces additional pollutants and expenses to these otherwise green and sustainable processes. Moreover, by taking advantage of the synergistic effect of thermal energy and charge carrier formation by light irradiation, black TiO_2 can be utilized for CO_2 hydrogenation under sacrificial reagent-free conditions. For instance, Jin et al. achieved a methane yield of 93.8% in photothermal CO_2 hydrogenation over Ru/black TiO_2 at temperatures below 300 °C, using a catalyst prepared by hydrogenating crystallized TiO_2 [15].

The crystal and electronic structures of TiO_2, as well as its catalytic activity, are significantly influenced by the preparation method. For instance, reducing crystalline TiO_2 through aluminothermic or electrochemical processes, or using reducing agents such as $NaBH_4$, can create a disordered TiO_2 shell around a crystalline TiO_2 core. The thickness of this reduced shell, along with its heterojunction with the crystalline core, plays a crucial role in determining the catalyst's activity and selectivity towards either CO or CH_4 during photocatalytic and photothermal CO_2 reduction in a sacrificial reagent-free environment [21–23]. Another approach for generating O_{VS} in TiO_2 involves chemical reduction using surfactants during synthesis. In this method, O_{VS} are distributed throughout the catalyst, from the surface to the bulk, and the resulting material exhibits a high degree of amorphicity, as evidenced by broad, low-intensity X-ray diffraction (XRD) peaks [24]. Density functional theory (DFT) simulations of amorphous reduced TiO_2 (AM-TiO_X) have demonstrated that, unlike in crystalline TiO_2 where O_{VS} are localized, the amorphization process disperses O_{VS} throughout the structure. This amorphization rearranges the atomic structure, making the O_V sites less distinct compared to those in crystalline TiO_2, where O_{VS} are more easily identifiable in the final structure [25]. Moreover, the electronic states in reduced TiO_2 are influenced by polarons. A recent study investigating the effect of polaron formation through the creation of oxygen vacancies in crystallized rutile showed that surface polarons enhance CO adsorption on 5-coordinated Ti atoms. In contrast, in the absence of surface polarons, CO readily desorbs from the surface. The adsorbed CO can interact with subsurface polarons, which may contribute to the reaction mechanism by enabling electron transfer to the adsorbate [26]. In the case of amorphous reduced TiO_2, an increased Ti/O ratio (approaching 1) is associated with expanded Ti coordination numbers (from 3 up to 7 [25]). This structural change leads to the formation of deep charge carrier traps, potentially limiting the ability of subsurface polarons to participate in surface reactions. Consequently, this could change the reaction mechanism and selectivity as compared to crystallized black TiO_2. To better understand how polarons affect the adsorption and activation of CO_2 in amorphous TiO_2 (AM-TiO_X), a detailed DFT analysis is recommended. Such an investigation could provide insights into how polaron dynamics influence reaction pathways, particularly under varying defect concentrations and surface conditions. In proposed mechanisms involving O_V sites in crystalline TiO_2, where oxygen vacancies are more localized and distinct, two common active modes of CO_2 adsorption have been suggested. In one mode, CO_2 adsorbs directly via its oxygen atom onto the O_V site, while in the other, CO_2 adsorbs in a bidentate mode on Ti atoms adjacent to the O_V. These different adsorption modes can significantly influence both the activation energy and selectivity in the photocatalytic reactions [27]. Adsorption modes that induce less symmetry in the CO_2 molecule can lower the energy barrier for accepting electrons, thereby activating the molecule for the reaction [28]. As a result, O_{VS} in crystalline metal oxide catalysts are regarded as highly active sites for CO_2 hydrogenation [29]. However, the impact of O_{VS} in amorphous, non-stoichiometric metal oxides on catalyst activity and selectivity remains largely unexplored.

In this study, we synthesized AM-TiO_X catalysts with different oxygen vacancy densities using a chemical reduction method. To achieve an amorphous structure while avoiding excessive reduction, SiO_2 was incorporated. Additionally, the incorporation of SiO_2 could help reduce particle agglomeration, thereby enhancing the specific surface area of the catalyst. The SiO_2 content was kept at approximately 10 wt.% to avoid surface exposure and minimize SiO_2-TiO_X interactions, which could affect catalytic activity. The catalyst's activity in both thermal and photo-assisted thermal CO_2 hydrogenation was investigated. A reaction mechanism was proposed based on *in situ* diffuse reflectance infrared Fourier transform spectroscopy (DRIFTS) of CO_2 hydrogenation, supported by DFT simulations of hydrogen mobility over amorphous TiO_2 with oxygen vacancies, to explain the high selectivity of this catalyst for carbon monoxide production, and the effect of visible light irradiation in CH_4 production enhancement. Catalyst stability was also examined, and the role of Ru in stability and reaction mechanisms was explored.

2 Experimental section

2.1 Materials

Titanium(IV) butoxide (98%, Sigma-Aldrich), ethanol (absolute for analysis, Sigma-Aldrich), ammonia 30% (PanReac AppliChem), hexadecyltrimethylammonium bromide (CTAB) (≥ 98%, Sigma-Aldrich), hydrochloric acid (37%, Sigma-Aldrich), silicon dioxide (nanopowder 5–15 nm, 99.5%, Sigma-Aldrich), Rutile TiO_2 nano powder (Sigma-Aldrich), and ruthenium(III) chloride hydrate (Tokyo Chemical Industry (TCI)) were used for the synthesis of catalysts as received without further purification.

2.2 Catalyst preparation

The synthesis method reported by Wang et al. [24], with slight modifications, was applied for the preparation of the black TiO_X catalysts. First, 5 mL of titanium(IV) butoxide was slowly added to 20 mL of ethanol while being magnetically stirred. Then, 0.75 mL of HCl was added to the solution. In a separate beaker, 0.5 g of CTAB was dissolved in a 10 mL ethanol/DI water (1:1 volume) solution. This latter solution was slowly added to the first solution while being stirred. After a yellow gel formed, 1.5 mL of ammonia was drop-fed into the yellow gel and left on a magnetic stirrer for 1 h resulting in a white gel. In a separate beaker, a precise amount of SiO_2 was added to a 100 mL solution of ethanol and deionized water (1:1 by volume) to achieve approximately 10 wt.% SiO_2 in the final catalyst. The mixture was then sonicated for 2 h. The white gel was then added to this latter solution and vigorously stirred for 2 h. The beaker was then placed in a pre-heated oven at 180 °C for 4 h. The resulting solid was finely crushed and calcined in a muffle furnace at 300 °C for 1 h with a heating ramp of 5 °C·min^{-1}. Finally, the resulting black powder was calcined at 400 °C for 1 h in a tubular furnace with N_2 gas flow, using a heating ramp of 5 °C·min^{-1}. This catalyst was labeled as AM-TiO_X. To synthesize a catalyst with a lower level of oxygen vacancies (O_V), the exact procedure was repeated, but with the weight of CTAB reduced to 0.25 g. The resulting catalyst was labeled as AM-L-TiO_X.

For the preparation of ruthenium-decorated AM-TiO_X, a calculated amount of AM-TiO_X powder was added to a 100 mL solution of ethanol/DI water (1:1 volume). A desired amount of ruthenium(III) chloride hydrate was then added to this beaker and stirred at room temperature for 1 h to achieve a 2 wt.% Ru decoration. The temperature of the solution was then increased to 70 °C and left on the hotplate while being stirred to evaporate the solvent. The resulting powder was crushed and calcined at 400 °C in a tubular furnace with N_2 gas flow, using a heating ramp of 5 °C·min^{-1}. This catalyst was labeled as AM-TiO_X-2%Ru.

To prepare Rutile TiO_2 decorated with 2 wt.% Ru as the reference catalyst for CO_2 hydrogenation, TiO_2 nanopowder was added to a beaker containing 100 mL of an ethanol/DI water solution (1:1 by volume). While magnetically stirring the mixture, a calculated amount of ruthenium(III) chloride hydrate was added. The resulting suspension was continuously stirred for 24 h. Subsequently, the mixture was dried in an oven at 80 °C overnight. The dried powder was then finely crushed and calcined in a muffle furnace at 400 °C for 2 h, with a heating ramp of 5 °C·min^{-1}. The final catalyst was labeled as TiO_2-2%Ru.

2.3 Characterization

The morphology of the catalyst was determined using both transmission electron microscopy (TEM, Talos F200) and scanning electron microscopy (SEM, Hitachi S-3400N), while the crystallinity and bulk composition were analyzed by TEM and SEM, respectively. Additionally, X-ray diffraction analysis was conducted using a Bruker D8 Advance equipped with a Cu anode, Kα1 (1.544 Å) irradiation, a 2θ range from 10° to 80°, and a scan rate of 0.02 °/min to determine the crystal structure of the catalysts. Electron paramagnetic resonance (EPR) was recorded using a Bruker EMXmicro spectrometer at 9.845 GHz. The ultraviolet–visible–near infrared ray (UV–Vis–NIR) absorption spectra were measured using a PerkinElmer Lambda 950 spectrophotometer. The N_2 adsorption–desorption isotherms were collected at −196 °C using a Micromeritics 3Flex 3500 series coupled with a Smart VacPrep system. The specific surface area was estimated using the Brunauer–Emmett–Teller (BET) theory, and the pore volume was calculated using the Barrett–Joyner–Halenda (BJH) method. The oxidation state of the elements on the surface of the synthesized catalysts was determined by X-ray photoelectron spectroscopy (XPS) using an AMICUS spectrometer with Mg Kα X-ray radiation (1253.6 eV) and Al Kα X-ray radiation (1486.6 eV) at 15 kV and 12 mA. X-ray absorption spectra (XAS) were collected in transmission mode in beamline BL1.1W: Multiple X-ray Techniques (MXT) of Synchrotron Light Research Institute (SLRI), Thailand.

In situ DRIFTS was conducted on a Bruker Invenio S spectrometer equipped with a liquid nitrogen-cooled MCT detector. The catalysts were loaded in a Praying Mantis HVC-DRP reaction chamber with ZnSe and glass windows. The catalysts were heated to 400 °C at a rate of 10 °C·min^{-1} under a nitrogen flow of 15 mL·min^{-1} and held at this temperature for 2 h prior to the reaction (the recorded spectrum at this step was used as the reference spectrum). For the AM-TiO_X-2%Ru catalyst, reduction was performed in a flow of hydrogen (13 mL·min^{-1}) and nitrogen (15 mL·min^{-1}) at 400 °C for 30 min (the reference spectrum for this catalyst was recorded at the end of the reduction step). Following the heat treatment, a gas stream containing CO_2 (3 mL·min^{-1}), H_2 (13 mL·min^{-1}), and N_2 (15 mL·min^{-1}) was introduced into the cell. The Fourier transform infrared (FTIR) spectra measured at specific intervals were subtracted from the reference spectra. A laser pointer with a wavelength of 405 nm was used for light irradiation through the glass window of the Praying Mantis reactor cell.

For NH_3 DRIFT analysis, the catalysts were heated to 400 °C with a heating ramp of 20 °C·min^{-1} and a N_2 flow rate of 20 mL·min^{-1} in the Praying Mantis reaction chamber. The catalysts were held at 400 °C for 2 h. After measuring the background spectra at 400 °C, the reaction chamber was cooled down to 350 °C and then to 40 °C for background measurement. The catalyst was saturated with NH_3 using a 15% NH_3/He gas flow for 30 min at 40 °C. Nitrogen gas with a 20 mL·min^{-1} flow rate was then fed into the reaction chamber to remove physically adsorbed ammonia before measuring the spectrum. Subsequently, the temperature was increased to 350 °C and then to 400 °C with a heating ramp of 10 °C·min^{-1} to measure the spectra.

Temperature-programmed desorption (TPD) was performed using a Micromeritics Autochem II 2920 Analyzer equipped with a thermal conductivity detector (TCD). First, 100 mg of catalyst was dried at 400 °C for 1 h under a helium gas stream. The adsorption of H_2 and CO_2 probe gases (for H_2-TPD and CO_2-TPD, respectively) was conducted at 40 °C for 1 h. After removing physically adsorbed probe gases from the catalysts with a constant stream of carrier gas and stabilizing the baseline, the desorption spectrum was recorded with a heating rate of 5 °C·min^{-1} from 40 to 800 °C.

2.4 CO_2 hydrogenation experiment

CO_2 hydrogenation experiments were conducted in the Praying Mantis HVC-DRP reaction chamber. A thin layer of catalyst was loaded into the reaction chamber. Prior to the CO_2 hydrogenation reaction, all catalysts were heat-treated for 2 h at 400 °C in a nitrogen gas stream. For the AM-TiO_X-2%Ru catalyst, a mixture of H_2/N_2 gas was used to reduce the catalyst for 30 min. CO_2 hydrogenation reactions were then carried out at 400, 350, 300, and 250 °C under stoichiometric methanation conditions (10 vol.%

CO_2, 40 vol.% H_2, and 50 vol.% N_2). The gas hourly space velocity (GHSV) of 21,200 h^{-1} was maintained constant for all catalysts. For light irradiation, a visible light laser pointer (405 nm) was used to focus the light on the catalyst through the glass window of the cell. The inlet and outlet gas streams were analyzed by manual injection into a GC-TCD (Shimadzu, GC-2014) equipped with a ShinCarbon ST column and a GC-FID (Shimadzu, GC-2030) equipped with a DB-5 column with online sampling. The detector and injector temperatures of the GC-TCD were set to 120 and 100 °C, respectively. The column temperature was held constant at 55 °C for 3 min, then increased to 240 °C at a rate of 10 °C·min^{-1}, with argon as the carrier gas. In the GC-FID, the injector and detector temperatures were set to 150 and 200 °C, respectively. The column temperature was held at 55 °C for 3 min, then raised to 70 °C at a heating rate of 10 °C·min^{-1} and held for 1 min. Subsequently, the column temperature was increased to 240 °C at a rate of 20 °C·min^{-1}, with helium as the carrier gas.

CO_2 conversion and CO selectivity were calculated using Eqs. (1) and (2), respectively

$$\text{CO}_2\ \text{conversion}\,(\%) = \frac{n(\text{CO}_2,\text{in}) - n(\text{CO}_2,\text{out})}{n(\text{CO}_2,\text{in})} \times 100\% \quad (1)$$

$$\text{CO selectivity}\,(\%) = \frac{m(\text{CO},\text{out})}{m(\text{CO},\text{out}) - m(\text{CH}_4,\text{out})} \times 100\% \quad (2)$$

where $n(CO_2, in)$ and $n(CO_2, out)$ are the molar concentrations of CO_2 in the feed and reactor outlet, respectively, and $m(CO, out)$ and $m(CH_4, out)$ are the molar production rates of CO and CH_4 in the reactor outlet.

2.5 Computational details

Theoretical calculations were conducted using BIOVIA Materials Studio 7.0. An amorphous TiO_2 structure was generated from an anatase TiO_2 supercell containing 48 atoms through the melt-quench method. The supercell was initially heated to 4726.85 °C at a rate of 117.5 K·ps^{-1} and maintained at this temperature for 40 ps. Subsequently, it was cooled to room temperature at a rate of 0.235 K·ps^{-1} and held for 10 ps. Simulations were performed with a 2 fs time step in an isobaric ensemble (NPT), using a Nosé-Hoover-Langevin (NHL) thermostat and barostat with time constants of 0.1 and 0.4 ps, respectively [30]. DFT optimization was carried out using the CASTEP module, employing the generalized gradient approximation (GGA) with the Perdew–Burke–Ernzerhof (PBE) functional and a plane-wave cut-off of 500 eV. For the projected density of states (PDOS) simulation in the CASTEP module, the amorphous structure from the previous step was reoptimized using the PBE functional at the GGA level. Ultrasoft pseudopotentials were used to represent the interaction between ions and electrons, with a plane-wave cut-off energy of 500 eV. The Brillouin zone was sampled with a 4 × 4 × 2 grid. Convergence criteria were set to a total energy difference of 1×10^{-5} Ha, a maximum force per atom of 0.002 Ha·$Å^{-1}$, and a maximum displacement between cycles of 0.005 Å. To achieve a better estimation of the bandgap, Hubbard terms with values of U_d = 11.0 eV and U_p = 1.0 eV were incorporated. For the PDOS simulation of amorphous TiO_2 with 50% oxygen vacancies, oxygen atoms were randomly deleted, and the structure was optimized using the aforementioned methods and parameters.

The hydrogen adsorption simulation was conducted using the DMol3 module by calculating the adsorption energy of hydrogen on amorphous TiO_2, both with and without one or two oxygen vacancies. Oxygen vacancies were introduced by removing oxygen atoms from the amorphous TiO_2 structure. For structural optimization and Gibbs free energy calculations in the DMol3 module, the GGA and Becke-Lee-Yang-Parr (BLYP) functional were employed. The relativistic effects of transition metals were accounted for using the DFT semi-core pseudopotential (DSPP) approach and the double numerical (DN) basis set. The convergence criteria for structural optimization were set as follows: a total energy difference of 1×10^{-5} Ha, a maximum force per atom of 0.002 Ha·$Å^{-1}$, a maximum displacement between cycles of 0.005 Å, and Monkhorst-Pack k-point sampling of 1 × 2 × 1. Adsorption energy was calculated using Eq. (3)

$$E_{\text{ad}} = E_{\text{H/sur}} - \frac{1}{2}E_{\text{H}_2} - E_{\text{sur}} \quad (3)$$

where E_{ad} is hydrogen adsorption energy, E_{sur} is energy of the bare surface, E_{H_2} is the energy of the hydrogen gas, and $E_{H/sur}$ is the energy of adsorbed hydrogen on the surface.

3 Results and discussion

Figure 1(a) presents the XRD spectra of the prepared samples. The spectra show a broad peak around 25°, indicating that the catalysts are amorphous. Similarly, the XRD spectrum of SiO_2 powder exhibits a broad peak near 23°, suggesting that these nanoparticles are also amorphous [31, 32]. The reduced intensity of the SiO_2 broad peak in the prepared samples could be attributed to the formation of a TiO_X shell around the SiO_2 nanoparticles [33]. Furthermore, the short-range order in the AM-TiO_X catalyst was studied using X-ray absorption near-edge structure (XANES). The resulting normalized Ti K-edge spectra of the sample, along with those of Anatase-TiO_2 and Rutile-TiO_2 as standards, are shown in Fig. 1(b). The pre-edge peaks in the AM-TiO_X XANES spectrum are labeled as A1, A2, A3, and B. The A1 peak is typically assigned to the quadrupole transition from the 1s core orbital to the 3d valence orbital. The A2, A3, and B peaks correspond to dipole transitions from the 1s core orbital to various components of 3d-4p hybridized states [34, 35]. The position and intensity of the A2 peak are particularly sensitive to interatomic bond distances, coordination numbers, and bond angles. As the crystallinity of the material decreases, the intensity of the A2 peak increases, reflecting stronger p-d hybridization due to local disorder around the Ti atoms [36–38]. Moreover, as disorder in the local atomic environment around Ti increases, the white line broadens, and its intensity decreases [39, 40]. XRD and XANES analyses confirm the absence of both long-range and short-range orders in the prepared sample.

Figure 1(c) presents the UV–Vis–NIR absorption spectra. All catalysts exhibit light absorption in both the visible and NIR regions. The AM-TiO_X sample shows higher absorption in the near-infrared region compared to the AM-L-TiO_X sample, which has a lower level of O_V. The black color and increased light absorption are attributed to the excitation of electrons from defect-induced energy states in the conduction band (CB) tail to the upper CB [25]. Thus, the higher absorption in both visible and NIR regions for AM-TiO_X can be attributed to its higher level of oxygen vacancies compared to AM-L-TiO_X. Additionally, the AM-TiO_X-2%Ru sample exhibits the highest absorption in both the visible and NIR regions. This enhanced light absorption can be attributed to several factors. Firstly, the metallic electronic structure of Ru introduces energy states within the bandgap, close to the CB, of AM-TiO_X [41].

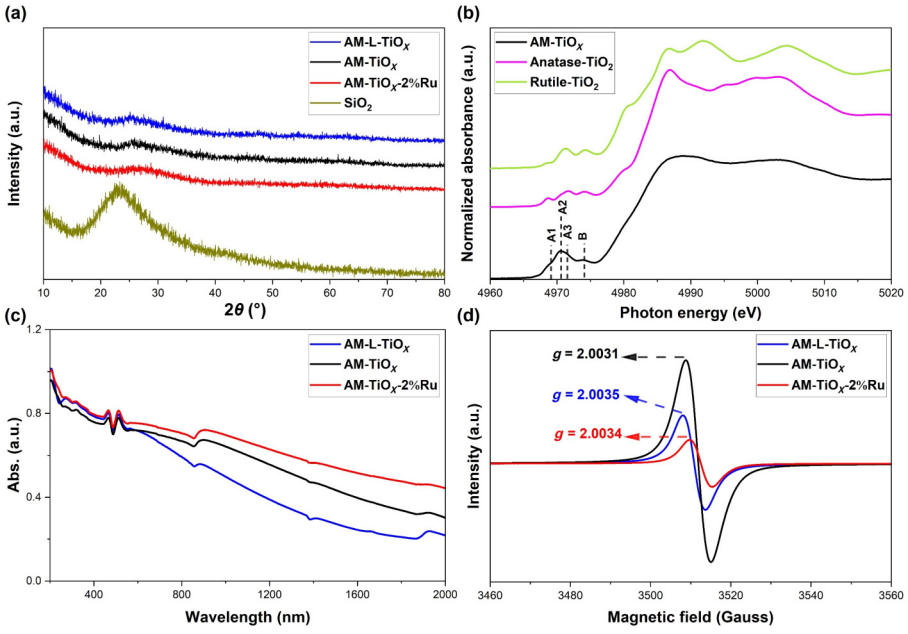

Figure 1 (a) XRD patterns of the prepared catalysts, (b) Ti K-edge XANES spectra of the AM-TiO$_X$ sample compared with Anatase and Rutile TiO$_2$ standards, (c) UV–Vis–NIR spectra, and (d) EPR spectra of all samples.

These new states facilitate increased light absorption. Furthermore, the localized surface plasmon resonance (LSPR) of the ruthenium oxide particles also contributes to enhanced light absorption across the visible to NIR regions [42–44].

EPR measurements were conducted to examine the presence of oxygen vacancies in the prepared samples, with the results shown in Fig. 1(d). The AM-TiO$_X$ sample exhibits the most intense EPR signal, with a *g*-value of approximately 2.0031. This *g*-value is commonly attributed to unpaired electrons trapped at O_V [45, 46], suggesting a higher concentration of O_{VS} in AM-TiO$_X$ compared to the other samples. The AM-L-TiO$_X$ shows a reduced EPR signal intensity and a slight *g*-value shift, indicating a lower O_V concentration and a modified local environment for the unpaired electrons [47]. The amorphous nature of the samples contributes to a wider range of possible defect sites and electronic environments.

The EPR spectrum of AM-TiO$_X$-2%Ru reveals a further decrease in the EPR signal, implying that the Ru decoration method has resulted in a reduction in the level of O_V.

Figure 2 shows the TEM images of the AM-TiO$_X$-2%Ru catalyst. The TEM analysis reveals that the nanostructure of the catalyst consists of agglomerated spherical particles. Additionally, the observed lattice fringes were measured, yielding a *d*-spacing of 0.300 to 0.319 nm, corresponding to the (110) plane of RuO_2 (referenced by XRD card: COD 96-100-0059). As the measured *d*-spacing does not match those of Anatase-TiO$_2$ (XRD card reference: COD 96-101-0943), Rutile-TiO$_2$ (XRD card reference: COD 96-900-1682), or Brookite TiO$_2$ (XRD card reference: COD 96-900-4138), it can be inferred that the TiO$_X$ is in an amorphous form.

The morphology and chemical composition of the prepared

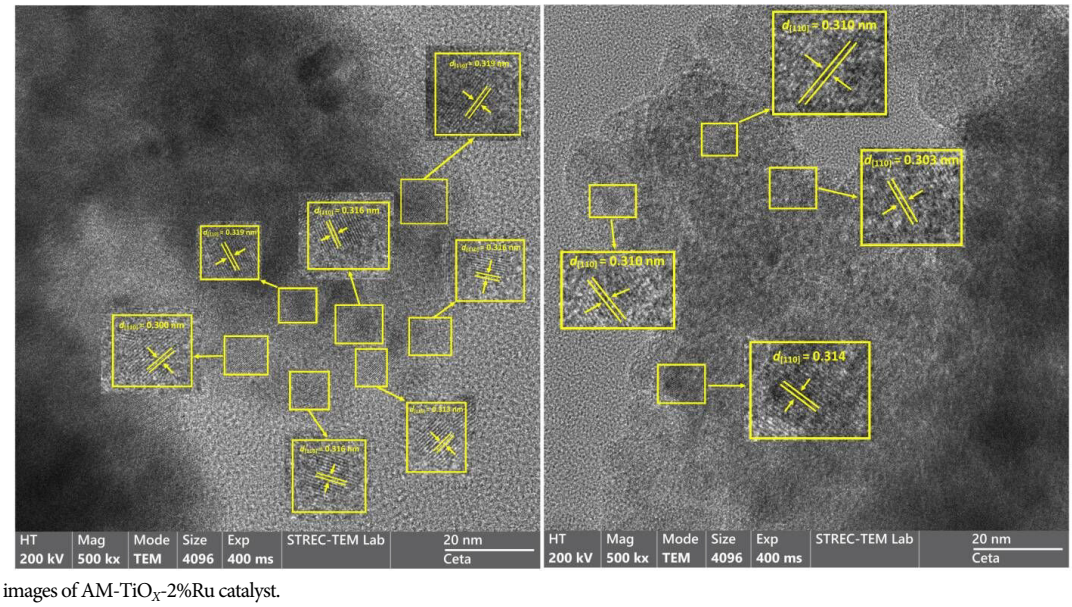

Figure 2 TEM images of AM-TiO$_X$-2%Ru catalyst.

catalysts were analyzed using SEM and energy-dispersive X-ray (EDX), as shown in Figs. S1 and S2 in the Electronic Supplementary Material (ESM). The SEM images reveal that the catalysts consist of agglomerated spherical particles. The EDX analysis indicates that the atomic ratio of Ti/O increases from the AM-L-TiO_X to the AM-TiO_X catalyst, suggesting a higher level of O_{VS} in the latter. Additionally, the elements are uniformly distributed across the catalysts, with the Ru concentration measured at 2 weight percent. Moreover, elemental composition analysis of the TiO_2-2%Ru catalyst reveals that Ru, comprising 2 wt.%, is uniformly distributed across the surface of the rutile TiO_2.

Figure S3 in the ESM shows the nitrogen adsorption–desorption isotherms, and the estimated specific surface area, pore size, and pore volume are reported in Table 1. All samples exhibit type IV isotherms with H_2 hysteresis, indicating a mesoporous structure [48]. Among them, AM-TiO_X has the highest BET specific surface area, but decoration with Ru significantly reduces this area, likely due to pore blockage by Ru particles.

XPS was conducted to investigate the surface composition and oxidation states of the elements in AM-L-TiO_X and AM-TiO_X catalysts, with the resulting spectra presented in Fig. 3. Two main peaks of Si with 2p and 2s excitation are reported to be positioned at around 99 and 149 eV [49–52], respectively, the absence of these two peaks in Figs. 3(a) and 3(d) (no peak was observed in around 100 to 200 eV region) confirms that Si is not on the surface of the catalysts. The deconvolution of the Ti 2p XPS spectrum of the AM-L-TiO_X sample revealed two characteristic peaks corresponding to Ti^{4+} at binding energies of 458.5 and 464.1 eV, along with two shoulders at 456.4 and 462.0 eV, which are attributed to an oxidation state of less than 4+ (represented as $Ti^{\delta+}$ in Fig. 3(b) with $\delta < 4$) [14, 53–55]. Similar peaks were observed in the deconvolution of the Ti 2p spectrum of AM-TiO_X (Fig. 3(e)). The O 1s spectrum of the AM-L-TiO_X catalyst (Fig. 3(c)) was fitted with three peaks at binding energies of 529.8, 531.8, and 533.5 eV, corresponding to lattice oxygen (O_L), Ti-OH (O_{OH}), and surface-adsorbed hydroxide complexes and water (O_S), respectively [21, 56–61]. Similar peaks were fitted to the O 1s spectrum of AM-TiO_X.

Table 1 Specific surface area, pore size, and pore volume of the prepared catalysts

Sample	BET surface area ($m^2 \cdot g^{-1}$)	Pore size (Å)	Pore volume ($cm^3 \cdot g^{-1}$)
AM-L-TiO_X	249.3	37.4	0.233
AM-TiO_X	333.5	35.9	0.299
AM-TiO_X-2%Ru	197.2	39.1	0.193

The type and strength of surface acidity significantly influence the mobility and adsorption of reactants, intermediates, and products during CO_2 hydrogenation [62]. Strong acid sites can enhance the binding strength of hydrogen and other intermediates on the catalyst surface, potentially saturating active sites and restricting the adsorption and activation of H_2. This limitation in hydrogen mobility and accessibility can significantly impact the catalyst's selectivity, potentially favoring reaction pathways that require fewer protons, such as CO formation, over those leading to CH_4 production. To investigate surface acidity and its sensitivity to light irradiation, NH_3 DRIFTS measurements were conducted at different temperatures. The resulting spectra are depicted in Fig. 4 for AM-L-TiO_X and AM-TiO_X, and Fig. 5 for AM-TiO_X-2%Ru. The observed bands in Fig. 4(a) at 1225 and 1600 cm^{-1} correspond to the symmetric and asymmetric bending vibrations of chemisorbed NH_3 on Lewis acid sites [63–68]. Peaks with high intensities are centered at 1403, 1438, 1667, and 1812 cm^{-1} (Fig. 4(a)), which are attributed to the asymmetric stretching vibration of N–H in NH_4^+ and the symmetric bending vibration of NH_4^+ on Brønsted acid sites [66–71], respectively, suggesting that

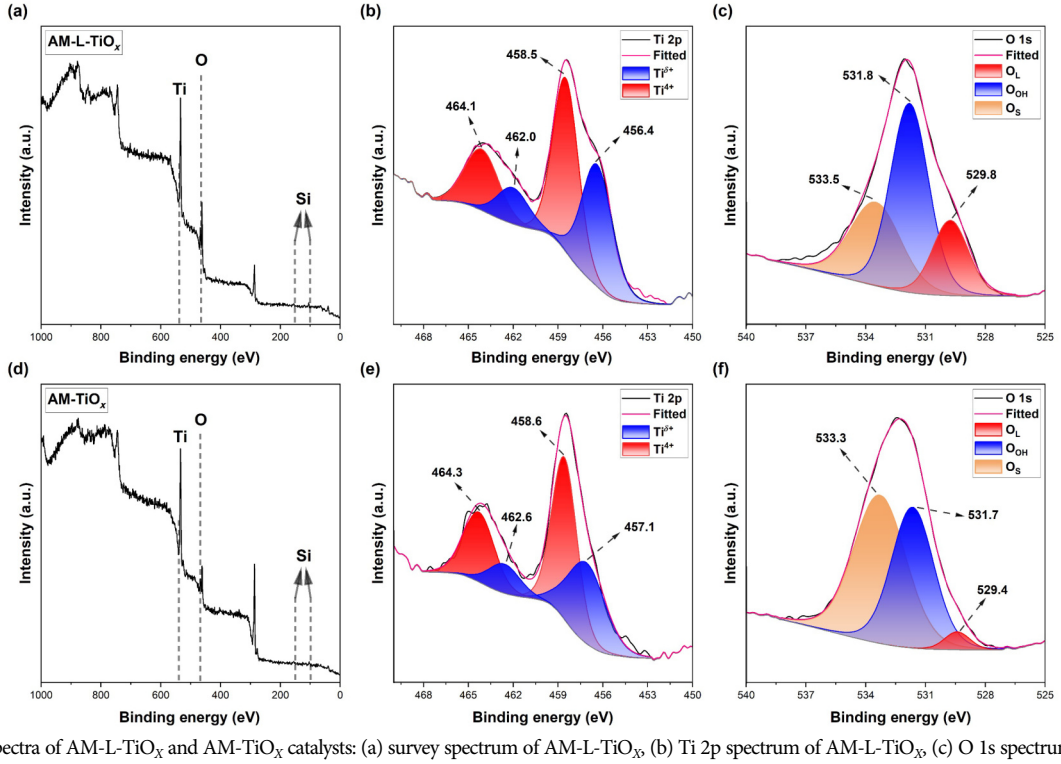

Figure 3 XPS spectra of AM-L-TiO_X and AM-TiO_X catalysts: (a) survey spectrum of AM-L-TiO_X, (b) Ti 2p spectrum of AM-L-TiO_X, (c) O 1s spectrum of AM-L-TiO_X, (d) survey spectrum of AM-TiO_X, (e) Ti 2p spectrum of AM-TiO_X, and (f) O 1s spectrum of AM-TiO_X.

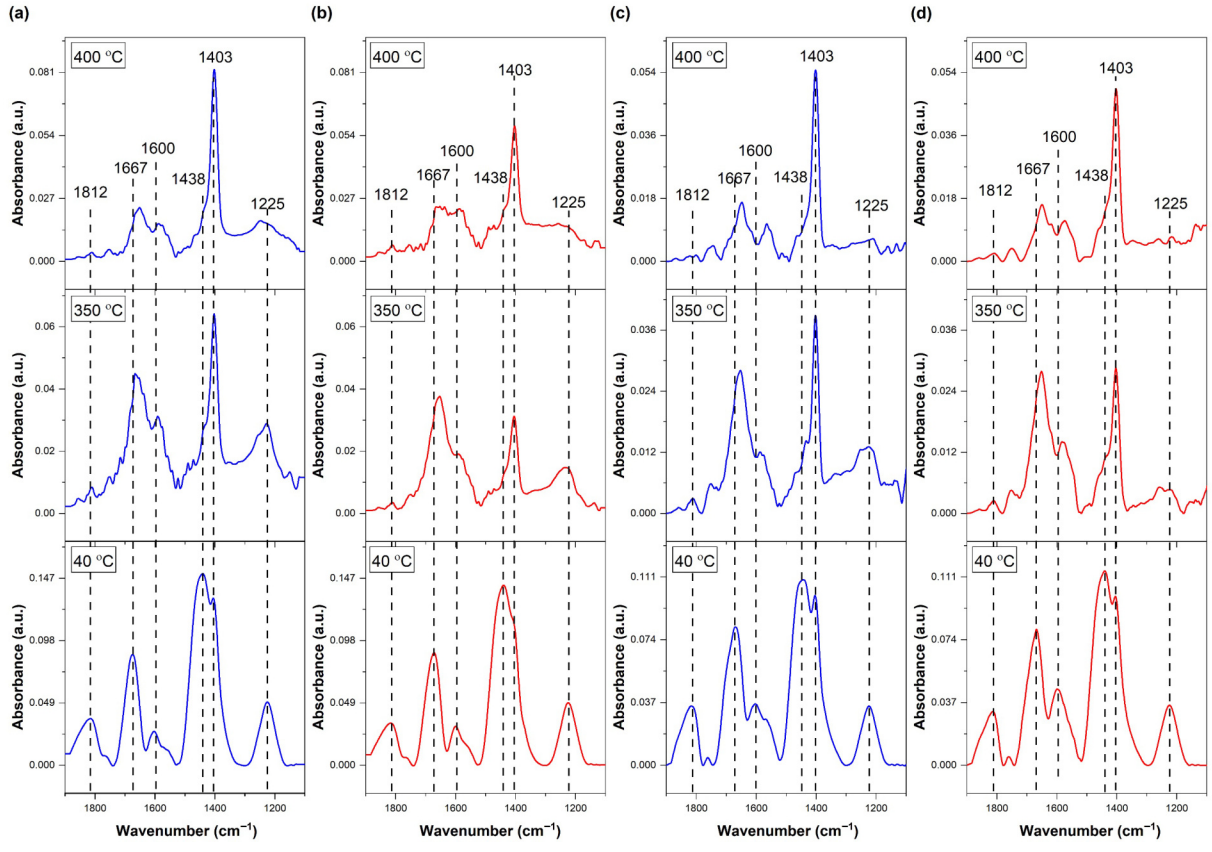

Figure 4 NH_3 DRIFT spectra of (a) AM-L-TiO_X without light irradiation, (b) AM-L-TiO_X under light irradiation, (c) AM-TiO_X without light irradiation, and (d) AM-TiO_X under light irradiation.

NH_3 primarily adsorbs on Brønsted acid sites. As the temperature increased from 40 to 350 °C, the intensity of the peaks decreased; however, the peaks corresponding to Brønsted acid sites exhibited the highest intensity. Further increasing the temperature to 400 °C revealed that NH_3 is primarily adsorbed on Brønsted acid sites at elevated temperatures (Fig. 4(a)). The same measurement was repeated for AM-L-TiO_X under light irradiation (Fig. 4(b)). At 40 °C, no difference in the peaks was observed between measurements with and without light illumination; however, the intensity of the peak at 1403 cm^{-1} measured at 350 and 400 °C was significantly reduced. Similar measurements were performed for the AM-TiO_X catalyst, with peak assignments shown in Figs. 4(c) and 4(d). For this catalyst, increasing the temperature to 350 and 400 °C, as well as exposure to light illumination, led to a slight decrease in the peak intensity at 1403 cm^{-1}. The effect of light irradiation on this catalyst is less pronounced compared to the AM-L-TiO_X catalyst. To explain the observed difference in the behavior of the catalysts under light irradiation, it is essential to consider the types and density of traps in reduced TiO_2 catalysts. Two common defects in reduced TiO_2 are O_V and $Ti^{\delta+}$ (Ti with an oxidation state of less than 4+). These defects can be present both on the surface and within the bulk of the material, depending on the catalyst's preparation method. Surface O_V can enhance photocatalytic activity by trapping electrons and activating reactants, while bulk O_V can improve the catalyst's light responsiveness, especially to visible and NIR light. Similarly, $Ti^{\delta+}$ defects can prolong the lifetime of photogenerated holes by trapping them, thereby further enhancing the photocatalytic activity of the material. However, a high density of these defects can have the opposite effect, significantly increasing the recombination of excited charge carriers and thereby reducing the diffusion length of electron-hole pairs [72, 73]. For example, in a study by Balog et al. [74] on the effect of defect density in reduced TiO_2 on its electronic and chemical properties, they prepared three TiO_2 catalysts with varying defect densities. Their photocurrent measurements revealed that the catalyst with the highest defect density (referred to as black TiO_2) exhibited the lowest current density, while the catalyst with the lowest defect density (referred to as white TiO_2) showed a substantially higher photocurrent. Notably, a sacrificial reagent was added to ensure that the oxidation reaction was not the limiting factor. In our case, the catalyst with a higher defect density (AM-TiO_X) is less responsive to light, likely due to the extensive recombination of charge carriers resulting from the higher density of defects.

Decorating AM-TiO_X with Ru enhances both the Lewis and Brønsted acidity of the catalyst, as shown in Fig. 5(a). Furthermore, a comparison between Figs. 5(a) and 5(b) reveals that light irradiation significantly impacts the acidity of the AM-TiO_X-2%Ru catalyst. Under light exposure and elevated temperatures, the peak at 1222 cm^{-1}, associated with Lewis acid sites, diminishes and becomes barely detectable at 400 °C. In contrast, the peak at 1403 cm^{-1}, indicative of Brønsted acid sites, sharpens and becomes the dominant feature in the spectrum at 400 °C. This phenomenon can be attributed to the formation and transfer of charge carriers. Upon illumination, electrons are excited into the conduction band, which mainly originates from Ti 3d orbitals, with contributions from O 2p orbitals [75, 76]. Due to the high defect density and short diffusion length of charge carriers in this catalyst, electrons near the metallic Ru can transfer to the Ru particles, increasing the

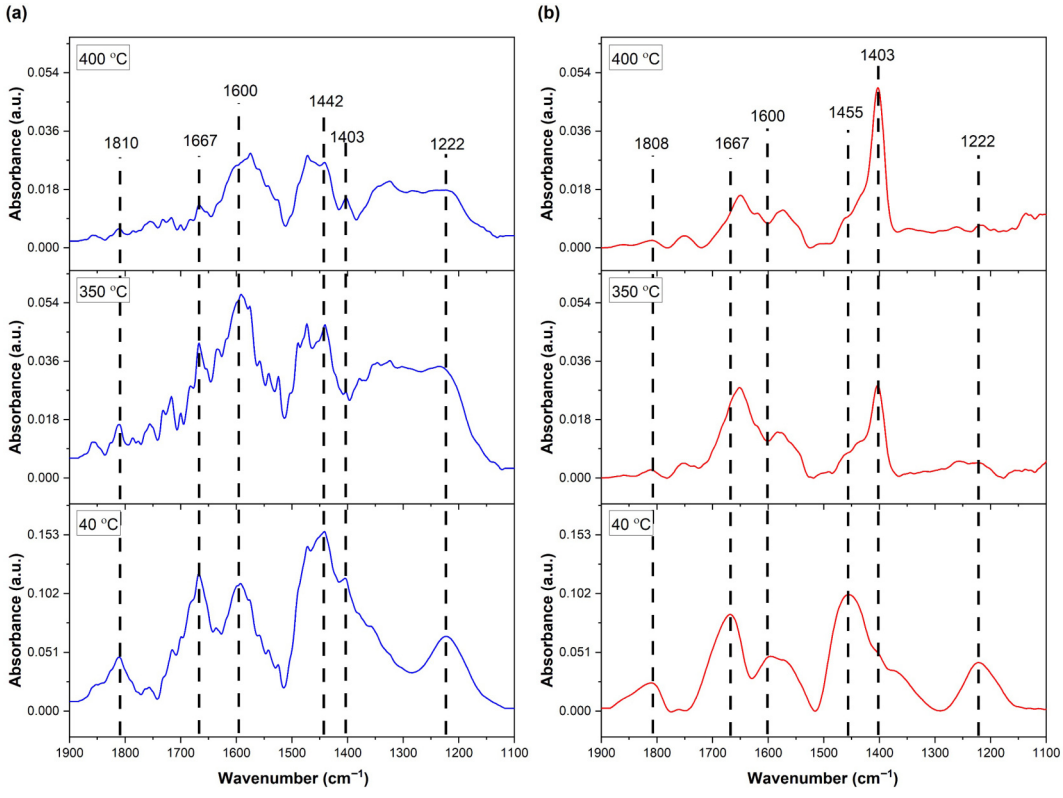

Figure 5 NH_3 DRIFT spectra of (a) AM-TiO_X-2%Ru without light irradiation and (b) AM-TiO_X-2%Ru under light irradiation.

electron density at Ru sites and thereby reducing both their Lewis and Brønsted acidity (Ru–H sites act as Brønsted acid sites). Simultaneously, some electrons remain in the Ti 3d orbitals, increasing the electron density around Ti atoms, further decreasing the number of effective Lewis acid sites. Additionally, the electron transfer to Ru generates more electron-deficient Ti sites near the Ru particles, which can withdraw electron density from neighboring OH groups. This withdrawal enhances the acidity of the protons in these OH groups, thereby increasing the Brønsted acidity, as reflected in the observed sharpening and dominance of the 1403 cm^{-1} peak at higher temperatures under light illumination (Fig. 5(b)).

The CO_2 adsorption capacity of all catalysts was evaluated using CO_2-TPD, with the results presented in Fig. 6(a). In the CO_2-TPD profiles, peaks observed between 50–200 °C are attributed to weak CO_2 adsorption sites, those between 200–400 °C to medium-strength sites, and peaks above 400 °C to strong adsorption sites [77, 78]. All catalysts exhibit strong adsorption sites, as indicated by the prominent peaks above 400 °C. A comparison between AM-TiO_X and AM-L-TiO_X shows that the intensity of the CO_2 desorption peaks around 250 °C (see Fig. S4 in the ESM) and above 400 °C (Fig. 6(a)) increases significantly with a higher density of O_{VS}, indicating enhanced adsorption capacity with increasing O_V density. However, when comparing AM-TiO_X with AM-TiO_X-2%Ru, the intensity of the shoulder peak around 250 °C is higher for AM-TiO_X, while the presence of Ru significantly enhances the intensity of the stronger CO_2 desorption peak above 400 °C. In addition, hydrogen adsorption behavior was measured, and the results are presented in Fig. 6(b). Similar to the CO_2-TPD profiles, hydrogen desorption peaks were observed at high temperatures in the H_2-TPD profiles, indicating strong hydrogen adsorption on the catalyst surface. Desorption peaks at around 90–300 °C are commonly attributed to the release of molecular hydrogen, while peaks above 300 °C are associated with dissociatively adsorbed hydrogen [79]. When comparing the H_2-TPD profiles of the AM-L-TiO_X and AM-TiO_X catalysts, similar peaks were observed. Both catalysts exhibited a peak at around 250 °C and two peaks at approximately 450 and 600 °C. The presence of these peaks suggests that hydrogen mobility on the surface is limited due to strong hydrogen adsorption. For the AM-TiO_X-2%Ru catalyst, a small shoulder peak shifts slightly towards higher temperatures (see Fig. S4 in the ESM), with a dominant peak appearing at around 550 °C. The intensity of this peak is the highest among the catalysts, suggesting the largest quantity of adsorbed hydrogen, despite this catalyst having the smallest specific surface area. Additionally, the interaction between Ru and the AM-TiO_X support significantly increases the strength of hydrogen adsorption, indicating that while hydrogen dissociation on Ru is facilitated, hydrogen mobility on the surface is restricted.

The results of the thermal and photothermal CO_2 hydrogenation reactions are presented in Fig. 7 for AM-L-TiO_X and AM-TiO_X, and in Fig. 8 for AM-TiO_X-2%Ru. Initial observations reveal that no products were formed at 250 °C for both AM-L-TiO_X and AM-TiO_X. However, increasing the temperature to 300 °C led to the formation of CO (15 $mmol{\cdot}h^{-1}{\cdot}g_{cat}^{-1}$) and CH_4 (1.2 $mmol{\cdot}h^{-1}{\cdot}g_{cat}^{-1}$) on the AM-L-$TiO_X$ catalyst, while only CO (14 $mmol{\cdot}h^{-1}{\cdot}g_{cat}^{-1}$) was detected for AM-$TiO_X$ at this temperature (Fig. 7). Repeating the experiments under light irradiation did not activate either catalyst at 250 °C but altered the selectivity at 300 °C. For AM-L-TiO_X, CO selectivity decreased to zero, while the CH_4 formation rate increased to 2 $mmol{\cdot}h^{-1}{\cdot}g_{cat}^{-1}$. In contrast, AM-$TiO_X$ exhibited a different behavior, as neither CO nor CH_4 was detected under light irradiation, indicating that this catalyst is less responsive to light. Therefore, light irradiation influences both the rate of product

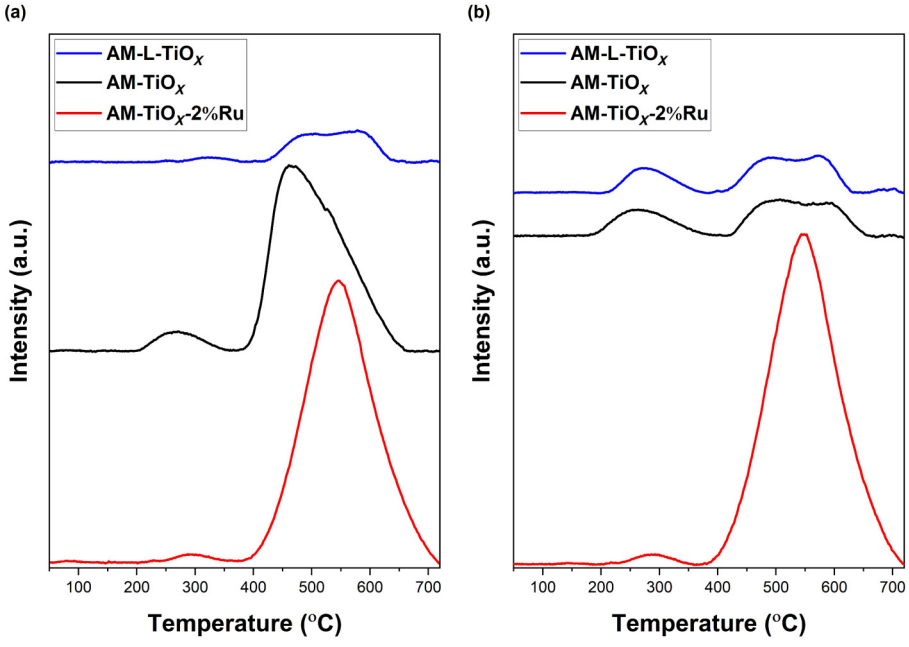

Figure 6 (a) CO_2-TPD and (b) H_2-TPD for all the catalysts.

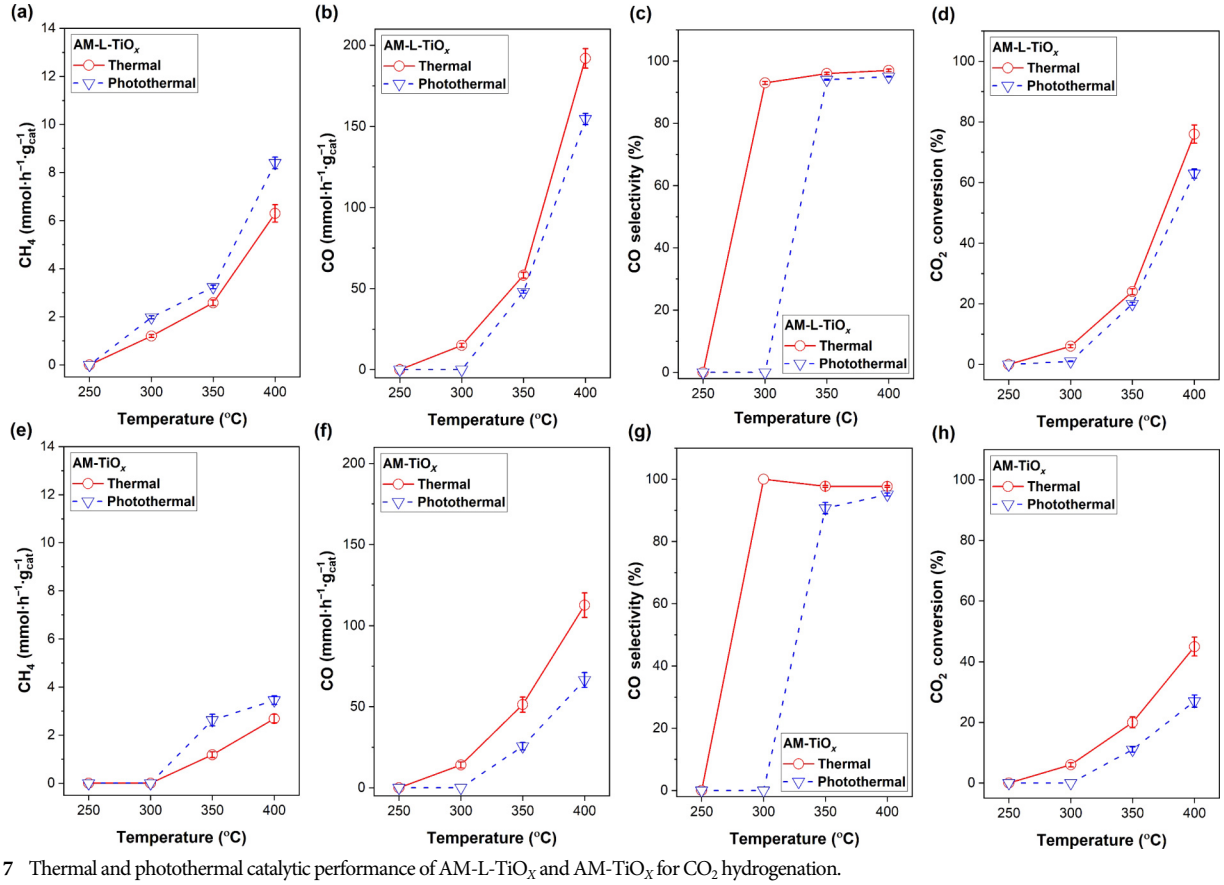

Figure 7 Thermal and photothermal catalytic performance of AM-L-TiO_X and AM-TiO_X for CO_2 hydrogenation.

formation and the selectivity of the catalysts. Based on the findings from NH_3-DRIFTS, CO_2-TPD, and H_2-TPD studies of the catalysts, the reaction temperature was increased to 350 °C. As shown in Fig. 7, this temperature-increase significantly enhanced the production rates of CH_4 and, particularly, CO for both catalysts. Repeating the experiment under light irradiation resulted in a decrease in the CO formation rate and an increase in the CH_4 formation rate for both catalysts. However, the reduction in CO production was more pronounced for the AM-TiO_X catalyst. Further increasing the temperature to 400 °C led to a substantial enhancement in the production rates of both CH_4 and CO for both catalysts. The highest CO production rate was 192 mmol·h^{-1}·g$_{cat}^{-1}$, while the highest CH_4 production rate was 6.3 mmol·h^{-1}·g$_{cat}^{-1}$, both observed for the AM-L-TiO_X catalyst. Regarding the effect of light

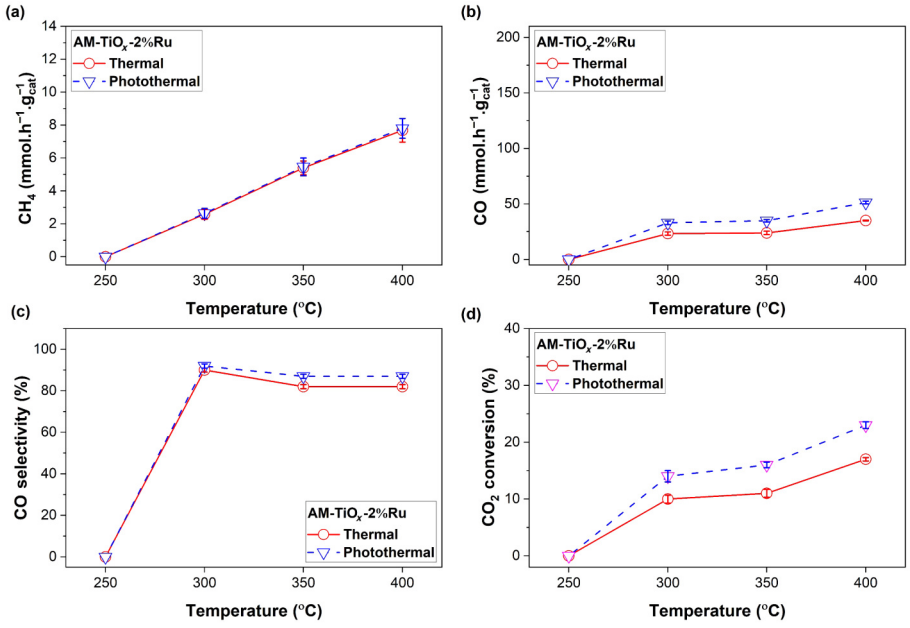

Figure 8 Thermal and photothermal catalytic performance of AM-TiO_X-2%Ru for CO_2 hydrogenation.

irradiation on both catalysts, CO production decreased, while CH_4 production increased. Additionally, the thermal CO_2 hydrogenation experiment at 400 °C was conducted using the TiO_2-2%Ru catalyst as a reference, with the results presented in Fig. S5 in the ESM. The CH_4 production rate of approximately 120 mmol·h^{-1}·g_{cat}^{-1} was achieved throughout the experiment, while the CO production rate was around 10 mmol·h^{-1}·g_{cat}^{-1}. This corresponds to a CO selectivity of roughly 8% for the TiO_2-2%Ru catalyst, which is significantly lower than the CO selectivity achieved with the amorphous TiO_X catalysts.

A distinct effect of light illumination on CH_4 and CO production rates is observed for the AM-TiO_X-2%Ru catalyst, as shown in Fig. 8. Unlike the AM-L-TiO_X and AM-TiO_X catalysts, light illumination does not affect the CH_4 production rate for AM-TiO_X-2%Ru (Fig. 8(a)), while it increases the CO production rate, exhibiting an opposite trend. This catalyst also demonstrates activity at temperatures higher than 250 °C, with CO selectivity decreasing below 90%. Given the significant difference in the specific surface areas of these catalysts (the BET surface area of AM-TiO_X-2%Ru is 197.2 m^2·g^{-1}, compared to 333.5 m^2·g^{-1} for AM-TiO_X), we normalized the CH_4 and CO production rates by the BET surface area to better illustrate the role of Ru. The normalized results are presented in Fig. S5 in the ESM. Notably, the AM-TiO_X-2%Ru catalyst exhibits the highest CH_4 production rate in both thermal and photothermal processes (Figs. S5(a) and S5(b) in the ESM). At 300 °C, this catalyst shows a higher CO production rate compared to the other catalysts. Furthermore, it achieves a comparable CO production rate to AM-L-TiO_X at 300 and 350 °C. Additionally, the CO production rate for AM-TiO_X-2%Ru slightly surpasses that of AM-TiO_X at 400 °C. All catalysts were also tested in a continuous photo-assisted reaction for 6 h at 400 °C to evaluate their stability, with results presented in Fig. S7 in the ESM. The formation rates of both CO and CH_4 decreased for the AM-L-TiO_X and AM-TiO_X catalysts, while the rates remained nearly constant for AM-TiO_X-2%Ru (these rates are not normalized by specific surface area). After the stability test, the used catalysts were characterized by EPR, as shown in Fig. S8 in the ESM. The AM-L-TiO_X and AM-TiO_X catalysts exhibited significant oxidation, whereas the AM-TiO_X-2%Ru catalyst showed slight reduction.

The kinetics of the CO_2 hydrogenation reaction were further analyzed using Arrhenius-type plots [80, 81], with the results presented in Fig. S8 and Table S1 in the ESM. A comparison of the apparent activation energy (E_a) for CH_4 formation revealed a significant decrease under photo-assisted thermal conditions for the AM-L-TiO_X and AM-TiO_X catalysts, while only a slight decrease was observed for the AM-TiO_X-2%Ru catalyst. For CO formation, a slight reduction in E_a was observed in the photo-assisted thermal process for the AM-L-TiO_X and AM-TiO_X catalysts. However, for the AM-TiO_X-2%Ru catalyst, the E_a for CO formation increased under photo-assisted thermal conditions. Overall, the AM-TiO_X-2%Ru catalyst exhibited the lowest E_a for CO_2 hydrogenation to CO.

The projected density of states (PDOS) for amorphous TiO_2 and amorphous TiO structures is shown in Fig. 9. A comparison between the DOS of amorphous TiO_2 and amorphous TiO reveals that the introduction of oxygen vacancies causes a shift in the VB edge away from the Fermi level. This shift suggests that the material can be excited by shorter wavelengths. The presence of O_V also leads to the formation of energy states in the CB tail, derived from the Ti 3d and O 2p orbitals. These defect-induced energy states act as recombination centers for charge carriers, resulting in a shorter diffusion length. Furthermore, the formation of Ti 3d and O 2p states in the CB tail indicates an increased electron density around Ti and O atoms, which can influence both hydrogen adsorption energy and the mode of CO_2 adsorption. Therefore, we simulated the hydrogen adsorption energy on amorphous TiO_2 with one and two oxygen vacancies, and the results are presented in Fig. 9(c). Notably, simulations on amorphous TiO (50% O_V) were unsuccessful, so we instead focused on amorphous TiO_2, introducing two oxygen vacancies by removing oxygen atoms. The simulation results indicate that increasing the number of oxygen vacancies enhances the stability of adsorbed hydrogen on the catalyst's surface. This enhancement in hydrogen adsorption energy can be explained by considering electron density redistribution on Ti and O atoms. The formation of O_{VS} increases the electron

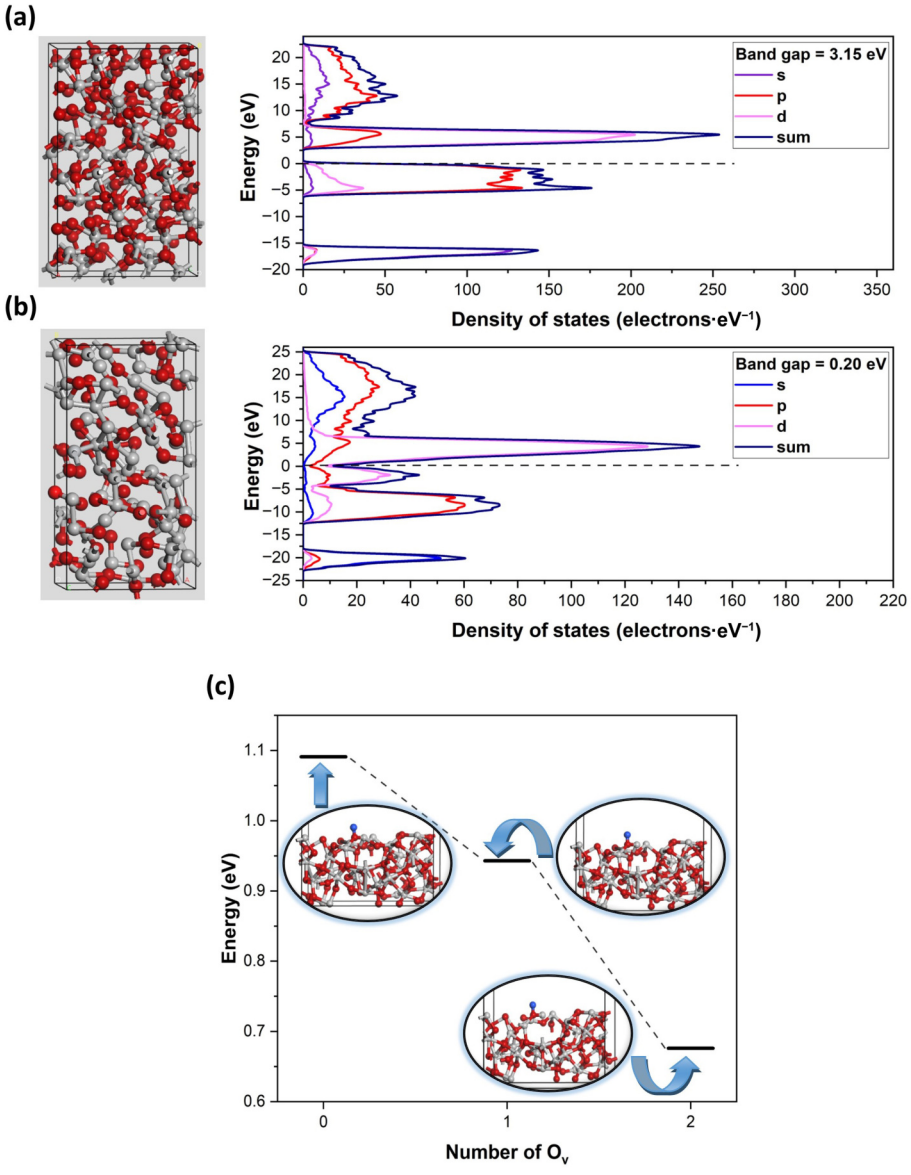

Figure 9 Projected density of states of (a) amorphous TiO_2, (b) amorphous TiO, and (c) adsorption energy profile of hydrogen on catalysts with and without oxygen vacancies.

density of the nearby Ti atoms. Due to the higher electronegativity of O atoms, electron density on Ti is partially redistributed to the adjacent oxygen atom, resulting in an increased electron density on the oxygen atom. This increase in electron density stabilizes the O–H bond.

To elucidate the mechanism of CO_2 hydrogenation over the prepared catalysts, we investigated the evolution of surface species during both thermal and photo-assisted thermal reactions using *in situ* FTIR spectroscopy. The corresponding spectra and band assignments are presented in Figs. 10 and 11. For the AM-L-TiO_X and AM-TiO_X catalysts (Fig. 10), the FTIR spectra in the range of 1100 to 1800 cm^{-1} indicate that monodentate bicarbonate (m-HCO_3*, 1400, 1444, and 1618 cm^{-1}), which forms via the chemisorption of CO_2 on hydroxyl groups, is the predominant intermediate species [82–89]. Additionally, two characteristic peaks of bicarbonate are observed at 3629 and 3594 cm^{-1} in the region above 3200 cm^{-1} (Fig. S9 in the ESM) [90]. The intensity of the m-HCO_3* band increases significantly over the course of the reaction, highlighting its role as the dominant intermediate species. A small peak at 1340 cm^{-1} is also observed, corresponding to the symmetric stretching vibration of the C–O bonds within formate species (HCOO*) [77, 91]. Additionally, the broad peak in the range of 1560 to 1655 cm^{-1} (more pronounced in Fig. 10(d)) likely results from overlapping bicarbonate and formate ions adsorbed on the surface, with the formate ion contributing a peak at 1640 cm^{-1} [27, 92, 93]. The more prominent shoulder within this range for AM-TiO_X correlates with the enhanced CH_4 formation rate under light irradiation. Moreover, a broad peak around 2800 cm^{-1} is evident for all catalysts, attributed to overlapping CH_3O* and HCOO* species [83, 94, 95] (Figs. 10 and 11). Characteristic peaks for gaseous CO are detected at 2113 and 2173 cm^{-1}, while the CH_4(g) band at 3015 cm^{-1} appears with very low intensity, consistent with the high selectivity of both AM-L-TiO_X and AM-TiO_X catalysts towards CO production [78, 86, 96, 97]. Similar measurements under light irradiation (Fig. 10 and Fig. S9 in the ESM) show that the detected intermediates and products are consistent with those observed in

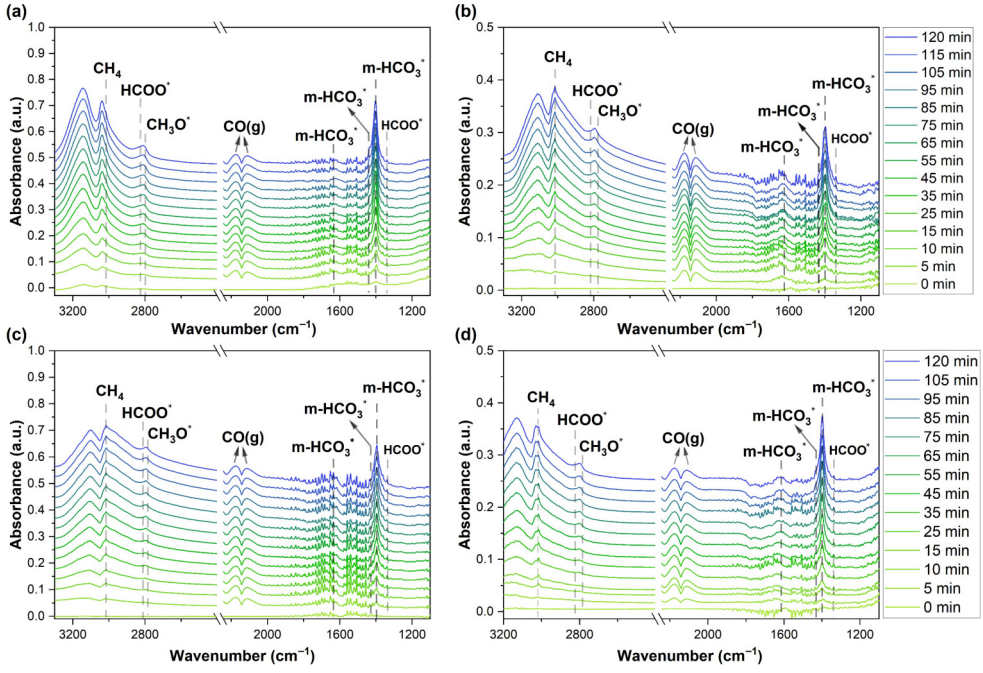

Figure 10 *In situ* DRIFT spectra of CO_2 hydrogenation at 400 °C over (a) AM-L-TiO_X without light irradiation, (b) AM-TiO_X without light irradiation, (c) AM-L-TiO_X under light irradiation, and (d) AM-TiO_X under light irradiation.

the absence of light, further confirming the reaction mechanism.

DRIFTS measurements of CO_2 hydrogenation, both with and without light illumination, were conducted on the AM-TiO_X-2%Ru catalyst, with the results shown in Fig. 11 and Fig. S10 in the ESM. Similar to the Ru-free catalysts, the m-HCO_3* species exhibited the highest intensity. A notable difference in the DRIFT spectra of this catalyst is the increased intensity of the broad peak in the range of 1560 to 1655 cm^{-1}, indicating a greater amount of formate ions (HCOO*) on the Ru-containing catalyst. This observation correlates with the higher rate of CH_4 production for this catalyst. Furthermore, a distinct formate (HCOO*) peak appears at 1750 cm^{-1} [93]. A small peak at 1304 cm^{-1}, observed under both reaction conditions, corresponds to the asymmetric stretching vibration of *CO_3^{2-} [98]. In addition, two new bands at 1910 and 2051 cm^{-1} were attributed to bridged and linear CO species adsorbed on Ru, respectively [95, 99, 100]. Measurements under light illumination did not lead to the formation of new intermediates. Thus, methane formation follows the formate pathway on all catalysts.

DRIFTS measurement of CO_2 hydrogenation over TiO_2-2%Ru (reference catalyst) was performed at 400 °C without light illumination. The resulting spectra, along with the assignment of active species, are provided in the Fig. S11 in the ESM.

To fully understand the reaction mechanism, it is essential to clarify how the catalyst's amorphous structure influences the formation of monodentate carbonate upon CO_2 adsorption. In crystalline metal oxides with low levels of oxygen vacancies, these vacancies are distinct and localized, making specific sites available for reactant interaction. In contrast, amorphous TiO_X catalysts with a near 1:1 Ti/O ratio exhibit a high concentration of oxygen vacancies, which results in a structural rearrangement that causes these vacancies to spread throughout the material rather than remain localized. This distribution affects how CO_2 interacts with the surface. Zhong et al. [25] demonstrated through simulations that in amorphous reduced TiO_X, a high oxygen vacancy concentration (up to 50%) significantly reduces the number of 6-coordinated Ti atoms, while 3- and 4-coordinated Ti atoms, as well as Ti–Ti pairs, increase. This suggests that the material redistributes its oxidation states to address its oxygen deficiency, potentially forming metal clusters as a stabilization mechanism. Upon CO_2 adsorption on the Lewis basic sites of amorphous TiO_X, the interaction between the negatively charged oxygen of the adsorbed CO_2 and the electron-rich Ti sites creates electrostatic repulsion. This repulsion decreases the

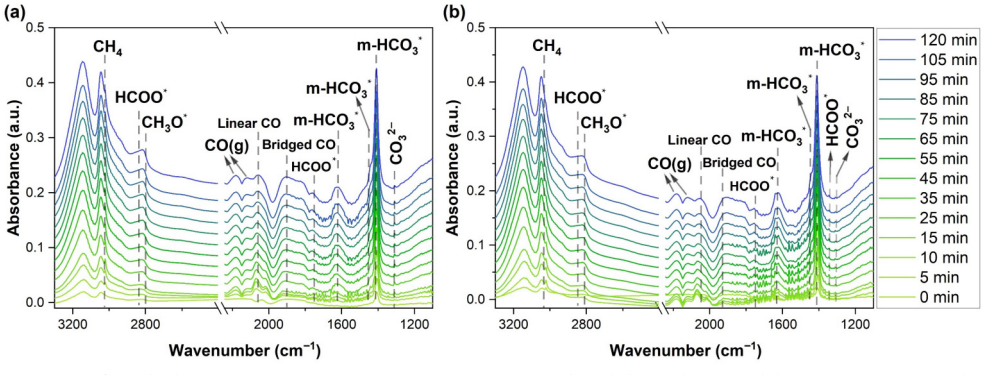

Figure 11 *In situ* DRIFT spectra of CO_2 hydrogenation at 400 °C over (a) AM-TiO_X-2%Ru without light irradiation and (b) AM-TiO_X-2%Ru under light irradiation.

likelihood that oxygen will coordinate with the electron-rich Ti, favoring monodentate rather than bidentate adsorption. As a result, monodentate adsorption is preferred on the amorphous TiO_X surface. Another important factor that can significantly affect the selectivity of the products is the strength of the hydrogen bond on the surface of the amorphous TiO_X. As shown by H_2-TPD experiments and DFT simulations on the hydrogen adsorption profile, hydrogen mobility is restricted due to the high stability of the O–H bond. Based on *in situ* DRIFT measurements, the CO_2 hydrogenation mechanism on amorphous TiO_X proceeds via two distinct reaction pathways, as depicted in Fig. 12. The first pathway (Fig. 12(a)) illustrates the mechanism on Ru-free surface sites or on active sites located away from Ru particles. Upon adsorption and initial hydrogenation of CO_2 on the catalyst surface, monodentate bicarbonate is identified as the primary active species, which subsequently undergoes further hydrogenation to form formate (HCOO*) species. The formate intermediate can then either decompose thermally or undergo additional hydrogenation to release CO and H_2O. Alternatively, a portion of the formate species can be hydrogenated further to yield methoxy (CH_3O*), which acts as a key intermediate in the pathway leading to CH_4 formation. In the final step, methoxy undergoes further hydrogenation steps to produce methane. Due to limited hydrogen mobility on the catalyst surface, attributed to strong hydrogen bonding, the reaction pathway favoring CO formation (which requires fewer hydrogenation steps) is more prevalent. When the catalyst is illuminated, photoexcitation causes electron transfer to Ti, which subsequently decreases the electron density of the oxygen atoms bonded to hydrogen. This reduction in electron density weakens the hydrogen bonds at these sites, thereby enhancing the mobility of hydrogen atoms. Increased hydrogen mobility means that more hydrogen is available for CO_2 hydrogenation, favoring the additional hydrogenation steps required for methane production over CO. Furthermore, the EPR analysis of the used catalysts indicates oxidation of the catalyst during the reaction. This oxidation is likely driven by strong interactions between CO_2 and the catalyst surface, which facilitate electron transfer from the catalyst to the adsorbed CO_2. This electron transfer can oxidize the catalyst and subsequently reduce its activity over time.

In the second reaction pathway (Fig. 12(b)), monodentate carbonate remains the primary intermediate species, similar to the previous mechanism. However, DRIFT analyses also reveal the presence of bridged and linear *CO species. These CO species likely result from the decomposition of formate intermediates, followed by subsequent adsorption on the Ru surface. Between the two forms, bridged CO is more stable due to its stronger binding on the catalyst, and it can undergo further hydrogenation to yield CH_4. The presence of Ru particles plays a critical role by facilitating hydrogen dissociation, thereby supplying the necessary hydrogen for methane formation. Additionally, under illumination, the CH_4 formation rate remains unchanged while the CO formation rate increases. This behavior is attributable to electron transfer to Ru upon excitation of the catalyst. The electron transfer weakens the Ru–CO bond, particularly affecting linearly adsorbed CO, which promotes its desorption and accounts for the enhanced CO formation rate in the photo-assisted reaction compared to the thermal process. Additionally, EPR analysis of the used AM-TiO_X-2%Ru catalyst (Fig. S12 in the ESM) shows a slight reduction after reaction, a result contrary to that of the Ru-free catalyst. The reduction can be attributed to the ability of Ru to effectively dissociate hydrogen, creating a locally reduced environment around Ru particles. This environment facilitates electron transfer from Ru to neighboring Ti atoms, reducing the TiO_X catalyst. Furthermore, protons generated on Ru can spill over onto the TiO_X, contributing to its reduction via water formation.

4 Conclusions

Amorphous TiO_X catalysts with two levels of O_V were prepared, and their performance in CO_2 hydrogenation under both thermal and photo-assisted thermal conditions was investigated. The effect of O_V on surface acidity, both with and without light illumination, was examined. Additionally, DFT simulations of hydrogen adsorption, together with H_2-TPD experiments, revealed restricted hydrogen mobility on the catalyst surface. *In situ* DRIFTS studies of CO_2 hydrogenation indicated that m-HCO_3* is the primary intermediate in the reaction, with subsequent hydrogenation to formate leading to high selectivity for CO production and only minimal CH_4 formation. Notably, the catalyst with the higher level of O_V showed lower activity for the formation of both products.

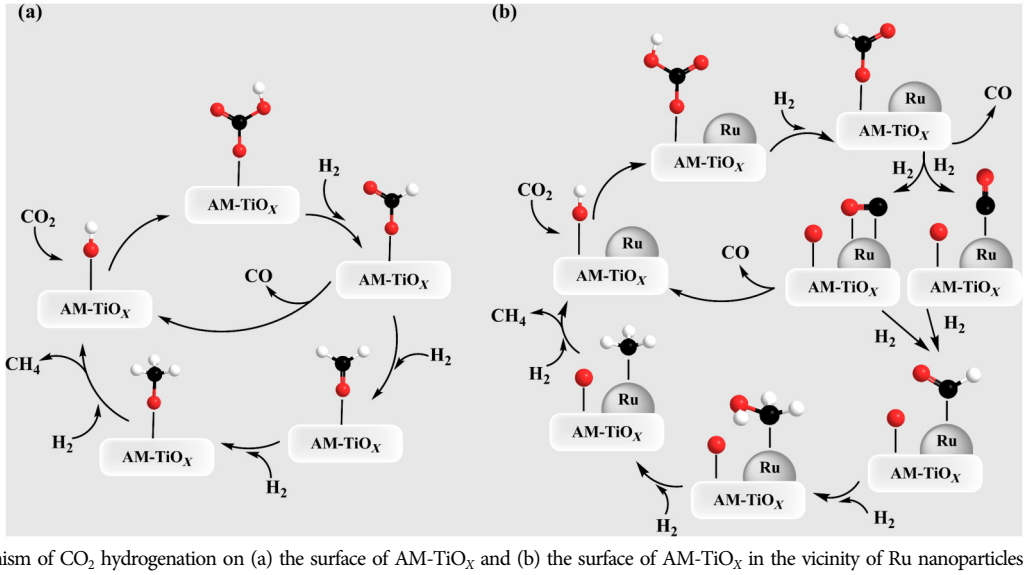

Figure 12 Mechanism of CO_2 hydrogenation on (a) the surface of AM-TiO_X and (b) the surface of AM-TiO_X in the vicinity of Ru nanoparticles (black: carbon, red: oxygen, and white: hydrogen).

The Ru-free catalysts, however, underwent oxidation and deactivation during the reaction. Decorating the catalyst with 2 wt.% Ru enhanced its stability and resulted in increased CH_4 formation, as Ru effectively facilitates hydrogen activation. The addition of Ru also influenced the reaction mechanism. DRIFTS analysis of the Ru-decorated catalyst showed the presence of bridged and linear CO species on Ru, which introduced additional pathways for both CO and CH_4 formation. We also observed that visible light irradiation of the Ru-free catalysts enhanced CH_4 production while significantly reducing CO formation. In contrast, light illumination had no effect on CH_4 production in the Ru-decorated catalyst but did enhance the CO production rate. This study provides valuable insights into the role of extensive levels of O_V on the electronic structure and atomic arrangement of metal oxides, offering a deeper understanding of the function and implications of oxygen vacancies in such materials.

Electronic Supplementary Material: Supplementary material (SEM-EDX analysis of all catalysts, along with the N_2 adsorption isotherms and EPR measurements of the used catalysts; additionally, the normalized experimental results and Arrhenius plots) is available in the online version of this article at https://doi.org/10.26599/NR.2025.94907218.

Data availability

All data needed to support the conclusions in the paper are presented in the manuscript and the Electronic Supplementary Material. Additional data related to this paper may be requested from the corresponding author upon request.

Acknowledgements

This research and innovation activity was supported by the Second Century Fund (C2F) of Chulalongkorn University, Thailand.

Declaration of competing interest

All the contributing authors report no conflict of interests in this work

Author contribution statement

M. F.: Experimental design, writing manuscript, data curation, validation. M. Y.: Experimental design, data curation. V. M.: Validation, data curation, experimental design, editing and review. C. V. P.: Validation, editing and review. M. S. V.: Validation, editing and review. S. P.: Validation, editing and review. P. P.: Project administration, validation, editing and review.

Use of AI statement

During the preparation of this work, the authors used Chatgpt and Gemini in order to correct the English grammar. After using this tool/service, the authors reviewed and edited the content as needed and take full responsibility for the content of the publication.

References

[1] Yang, F. F.; Zhang, T. Y.; Zhao, J. K.; Xiao, J. W.; Zhou, W. Tuning selectivity of CO_2 hydrogenation over Co catalysts by surface decoration of Sn. *J. Catal.* **2024**, *429*, 115242.

[2] Tawalbeh, M.; Javed, R. M. N.; Al-Othman, A.; Almomani, F.; Ajith, S. Unlocking the potential of CO_2 hydrogenation into valuable products using noble metal catalysts: A comprehensive review. *Environ. Technol. Innov.* **2023**, *31*, 103217.

[3] Nagireddi, S.; Agarwal, J. R.; Vedapuri, D. Carbon dioxide capture, utilization, and sequestration: Current status, challenges, and future prospects for global decarbonization. *ACS Eng. Au* **2024**, *4*, 22–48.

[4] Li, J. W.; Zeng, H. L.; Dong, X.; Ding, Y. M.; Hu, S. P.; Zhang, R. H.; Dai, Y. Z.; Cui, P. X.; Xiao, Z.; Zhao, D. H. et al. Selective CO_2 electrolysis to CO using isolated antimony alloyed copper. *Nat. Commun.* **2023**, *14*, 340.

[5] Wang, H. N.; Zou, Y. H.; Sun, H. X.; Chen, Y. F.; Li, S. L.; Lan, Y. Q. Recent progress and perspectives in heterogeneous photocatalytic CO_2 reduction through a solid-gas mode. *Coord. Chem. Rev.* **2021**, *438*, 213906.

[6] Xiao, C. L.; Zhang, J. Architectural design for enhanced C_2 product selectivity in electrochemical CO_2 reduction using Cu-based catalysts: A review. *ACS Nano* **2021**, *15*, 7975–8000.

[7] Xiao, Z. R.; Li, P.; Zhang, H.; Zhang, S. L.; Tan, X. Y.; Ye, F.; Gu, J. M.; Zou, J. J.; Wang, D. S. A comprehensive review on photo-thermal co-catalytic reduction of CO_2 to value-added chemicals. *Fuel* **2024**, *362*, 130906.

[8] Fan, W. K.; Tahir, M. Recent developments in photothermal reactors with understanding on the role of light/heat for CO_2 hydrogenation to fuels: A review. *Chem. Eng. J.* **2022**, *427*, 131617.

[9] Lv, C. C.; Bai, X. H.; Ning, S. B.; Song, C. X.; Guan, Q. Q.; Liu, B.; Li, Y. G.; Ye, J. H. Nanostructured materials for photothermal carbon dioxide hydrogenation: Regulating solar utilization and catalytic performance. *ACS Nano* **2023**, *17*, 1725–1738.

[10] Zhou, J.; Liu, H.; Wang, H. Q. Photothermal catalysis for CO_2 conversion. *Chin. Chem. Lett.* **2023**, *34*, 107420.

[11] Zhang, F.; Li, Y. H.; Qi, M. Y.; Yamada, Y. M. A.; Anpo, M.; Tang, Z. R.; Xu, Y. J. Photothermal catalytic CO_2 reduction over nanomaterials. *Chem Catal.* **2021**, *1*, 272–297.

[12] Jiang, W. B.; Loh, H.; Low, B. Q. L.; Zhu, H. J.; Low, J.; Heng, J. Z. X.; Tang, K. Y.; Li, Z. B.; Loh, X. J.; Ye, E. Y. et al. Role of oxygen vacancy in metal oxides for photocatalytic CO_2 reduction. *Appl. Catal. B: Environ.* **2023**, *321*, 122079.

[13] Huang, Y. M.; Yu, Y.; Yu, Y. F.; Zhang, B. Oxygen vacancy engineering in photocatalysis. *Solar RRL* **2020**, *4*, 2000037.

[14] Zhang, W.; Xue, J. B.; Shen, Q. Q.; Jia, S. F.; Gao, J. Q.; Liu, X. G.; Jia, H. S. Black single-crystal TiO_2 nanosheet array films with oxygen vacancy on {001} facets for boosting photocatalytic CO_2 reduction. *J. Alloys Compd.* **2021**, *870*, 159400.

[15] Jin, B. B.; Ye, X.; Zhong, H.; Jin, F. M.; Hu, Y. H. Enhanced photocatalytic CO_2 hydrogenation with wide-spectrum utilization over black TiO_2 supported catalyst. *Chin. Chem. Lett.* **2022**, *33*, 812–816.

[16] Zhang, Y. P.; Han, W.; Yang, Y.; Zhang, H. Y.; Wang, Y.; Wang, L.; Sun, X. J.; Zhang, F. M. S-scheme heterojunction of black TiO_2 and covalent-organic framework for enhanced photocatalytic hydrogen evolution. *Chem. Eng. J.* **2022**, *446*, 137213.

[17] Ji, M.; Kim, J. H.; Jeon, H. Y.; Han, S.; Lee, D. H.; Lee, Y. I. High-performance interfacial water evaporation of black TiO_{2-x} with high-concentration bulk oxygen vacancies. *Chem. Eng. J.* **2024**, *483*, 149435.

[18] Rajaraman, T. S.; Parikh, S. P.; Gandhi, V. G. Black TiO_2: A review of its properties and conflicting trends. *Chem. Eng. J.* **2020**, *389*, 123918.

[19] Wang, B.; Shen, S. H.; Mao, S. S. Black TiO_2 for solar hydrogen conversion. *J. Materiomics* **2017**, *3*, 96–111.

[20] Qian, C.; Liu, H. M.; Li, H. Y.; Wang, T.; Wang, S. Mesoporous TiO_2 spheres with rich oxygen vacancies for enhanced photocatalytic hydrogen production. *Int. J. Hydrogen Energy* **2024**, *51*, 605–614.

[21] Gao, J. Q.; Shen, Q. Q.; Guan, R. F.; Xue, J. B.; Liu, X. G.; Jia, H. S.; Li, Q.; Wu, Y. C. Oxygen vacancy self-doped black TiO_2

nanotube arrays by aluminothermic reduction for photocatalytic CO_2 reduction under visible light illumination. *J. CO_2 Util.* **2020**, *35*, 205–215.

[22] Santos, J. S.; Fereidooni, M.; Márquez, V.; Paz-López, C. V.; Villanueva, M. S.; Buijnsters, J. G.; Praserthdam, S.; Praserthdam, P. Photoactivity of amorphous and crystalline TiO_2 nanotube arrays (TNA) films in gas phase CO_2 reduction to methane with simultaneous H_2 production. *Environ. Res.* **2024**, *244*, 117919.

[23] Li, Y.; Zeng, Z. J.; Zhang, Y. M.; Chen, Y.; Wang, W. J.; Xu, X. M.; Du, M. Y.; Li, Z. S.; Zou, Z. G. Deactivation and stabilization mechanism of photothermal CO_2 hydrogenation over black TiO_2. *ACS Sustainable Chem. Eng.* **2022**, *10*, 6382–6388.

[24] Wang, T.; Li, W. W.; Xu, D. D.; Wu, X. M.; Cao, L. W.; Meng, J. X. A novel and facile synthesis of black TiO_2 with improved visible-light photocatalytic H_2 generation: Impact of surface modification with CTAB on morphology, structure and property. *Appl. Surf. Sci.* **2017**, *426*, 325–332.

[25] Zhong, J.; Xu, Z. T.; Lu, J.; Li, Y. Y. Precise electronic structures of amorphous solids: Unraveling the color origin and photocatalysis of black titania. *J. Phys. Chem. C* **2023**, *127*, 7268–7274.

[26] Cheng, C.; Zhu, Y. H.; Fang, W. H.; Long, R.; Prezhdo, O. V. CO adsorbate promotes polaron photoactivity on the reduced rutile TiO_2(110) Surface. *JACS Au* **2022**, *2*, 234–245.

[27] Kharade, A. K.; Chang, S. M. Contributions of abundant hydroxyl groups to extraordinarily high photocatalytic activity of amorphous titania for CO_2 reduction. *J. Phys. Chem. C* **2020**, *124*, 10981–10992.

[28] Chang, X. X.; Wang, T.; Gong, J. L. CO_2 photo-reduction: Insights into CO_2 activation and reaction on surfaces of photocatalysts. *Energy Environ. Sci.* **2016**, *9*, 2177–2196.

[29] Wang, X. H.; Lu, L.; Wang, B.; Xu, Z.; Xin, Z. Y.; Yan, S. C.; Geng, Z. R.; Zou, Z. G. Frustrated lewis pairs accelerating CO_2 reduction on oxyhydroxide photocatalysts with surface lattice hydroxyls as a solid-state proton donor. *Adv. Funct. Mater.* **2018**, *28*, 1804191.

[30] Paz, C. V.; Fereidooni, M.; Praserthdam, P.; Santiago, A. A.; Praserthdam, S.; Marquez, V. Toward the understanding of surface phenomena involved in the photocatalytic performance of amorphous TiO_2/SiO_2 catalyst-A theoretical and experimental study. *Appl. Surf. Sci.* **2022**, *588*, 152920.

[31] Fereidooni, M.; Núñez, O.; Márquez, V.; Paz, C. V.; Villanueva, M. S.; Tun, M. Z.; Kanjanaboos, P.; Praserthdam, S.; Praserthdam, P. Effect of substrate conductivity on charge transfer and CO_2 photoreduction in water vapor over silica-modified TiO_2 films. *Appl. Surf. Sci.* **2023**, *611*, 155595.

[32] Hu, X. L.; Li, C. Q.; Song, J. Y.; Zheng, S. L.; Sun, Z. M. Multidimensional assembly of oxygen vacancy-rich amorphous TiO_2-BiOBr-sepiolite composite for rapid elimination of formaldehyde and oxytetracycline under visible light. *J. Colloid Interface Sci.* **2020**, *574*, 61–73.

[33] Yang, H. Y.; Zhou, J. Y.; Duan, Z. J.; Liu, X.; Deng, B.; Fang, J.; Xu, W. L. Amorphous TiO_2 beats P25 in visible light photo-catalytic performance due to both total-internal-reflection boosted solar photothermal conversion and negative temperature coefficient of the forbidden bandwidth. *Appl. Catal. B: Environ.* **2022**, *310*, 121299.

[34] Dorosheva, I. B.; Kremneva, A. M.; Kaichev, V. V.; Valeeva, A. A.; Rempel, A. A. XAS study of sol-gel synthesized amorphous and anatase TiO_2 nanoparticles. *Mendeleev Commun.* **2024**, *34*, 224–225.

[35] Luca, V.; Djajanti, S.; Howe, R. F. Structural and electronic properties of sol-gel titanium oxides studied by X-ray absorption spectroscopy. *J. Phys. Chem. B* **1998**, *102*, 10650–10657.

[36] Triana, C. A.; Araujo, C. M.; Ahuja, R.; Niklasson, G. A.; Edvinsson, T. Electronic transitions induced by short-range structural order in amorphous TiO_2. *Phys. Rev. B* **2016**, *94*, 165129.

[37] Deng, H.; Yuan, L. Y.; Li, Z. J.; Wang, D. G.; Wang, X. C.; Liang, P. L.; Wang, L.; Liu, Y. C.; Fu, Y. J.; Chang, Z. Y. et al. A hybrid amorphous/crystalline TiO_2 material with enhanced photocatalytic performance. *Adv. Sustainable Syst.* **2022**, *6*, 2200316.

[38] Yadav, A. K.; Haque, S. M.; Shukla, D. K.; Phase, D. M.; Jha, S. N.; Bhattacharyya, D. Local structural investigations of Fe-doped TiO_2 amorphous thin films. *Thin Solid Films* **2020**, *716*, 138435.

[39] Li, J.; Liu, J.; Sun, Q.; Banis, M. N.; Sun, X. L.; Sham, T. K. Tracking the effect of sodium insertion/extraction in amorphous and anatase TiO_2 nanotubes. *J. Phys. Chem. C* **2017**, *121*, 11773–11782.

[40] Carta, D.; Mountjoy, G.; Regoutz, A.; Khiat, A.; Serb, A.; Prodromakis, T. X-ray absorption spectroscopy study of TiO_{2-x} thin films for memory applications. *J. Phys. Chem. C* **2015**, *119*, 4362–4370.

[41] Yuan, C. F.; Shen, Y. L.; Zhu, C. Y.; Zhu, P.; Yang, F.; Liu, J. H.; An, C. H. Ru single-atom decorated black TiO_2 nanosheets for efficient solar-driven hydrogen production. *ACS Sustainable Chem. Eng.* **2022**, *10*, 10311–10317.

[42] Ding, X. G.; Liow, C. H.; Zhang, M. X.; Huang, R. J.; Li, C. Y.; Shen, H.; Liu, M. Y.; Zou, Y.; Gao, N.; Zhang, Z. J. et al. Surface plasmon resonance enhanced light absorption and photothermal therapy in the second near-infrared window. *J. Am. Chem. Soc.* **2014**, *136*, 15684–15693.

[43] Min, B. K.; Nguyen, V. T.; Kim, S. J.; Yi, Y.; Choi, C. G. Surface plasmon resonance-enhanced near-infrared absorption in single-layer MoS_2 with vertically aligned nanoflakes. *ACS Appl. Mater. Interfaces* **2020**, *12*, 14476–14483.

[44] Bang, S.; Lee, S.; Park, T.; Ko, Y.; Shin, S.; Yim, S. Y.; Seo, H.; Jeon, H. Dual optical functionality of local surface plasmon resonance for RuO_2 nanoparticle-ZnO nanorod hybrids grown by atomic layer deposition. *J. Mater. Chem.* **2012**, *22*, 14141–14148.

[45] Foo, C.; Li, Y. Y.; Lebedev, K.; Chen, T. Y.; Day, S.; Tang, C.; Tsang, S. C. E. Characterisation of oxygen defects and nitrogen impurities in TiO_2 photocatalysts using variable-temperature X-ray powder diffraction. *Nat. Commun.* **2021**, *12*, 661.

[46] Dong, J. Y.; Han, J.; Liu, Y. S.; Nakajima, A.; Matsushita, S.; Wei, S. H.; Gao, W. Defective black TiO_2 synthesized via anodization for visible-light photocatalysis. *ACS Appl. Mater. Interfaces* **2014**, *6*, 1385–1388.

[47] Fittipaldi, M.; Gatteschi, D.; Fornasiero, P. The power of EPR techniques in revealing active sites in heterogeneous photocatalysis: The case of anion doped TiO_2. *Catal. Today* **2013**, *206*, 2–11.

[48] Behnajady, M. A.; Eskandarloo, H.; Modirshahla, N.; Shokri, M. Investigation of the effect of sol–gel synthesis variables on structural and photocatalytic properties of TiO_2 nanoparticles. *Desalination* **2011**, *278*, 10–17.

[49] He, H. Y.; Barr, T. L.; Klinowski, J. ESCA studies of framework silicates with the sodalite structure. 2. Ultramarine. *J. Phys. Chem.* **1994**, *98*, 8124–8127.

[50] Du, H. H.; Tressler, R. E.; Spear, K. E.; Pantano, C. G. Oxidation studies of crystalline CVD silicon nitride. *J. Electrochem. Soc.* **1989**, *136*, 1527–1536.

[51] Kaur, A.; Chahal, P.; Hogan, T. Selective fabrication of SiC/Si diodes by excimer laser under ambient conditions. *IEEE Electron Device Lett.* **2016**, *37*, 142–145.

[52] Puppin, E.; Lindau, I.; Abbati, I. Photoemission core level shifts in Gd silicides. *Solid State Commun.* **1991**, *77*, 983–986.

[53] Billo, T.; Fu, F. Y.; Raghunath, P.; Shown, I.; Chen, W. F.; Lien, H. T.; Shen, T. H.; Lee, J. F.; Chan, T. S.; Huang, K. Y. et al. Artificial photosynthesis: Ni-nanocluster modified black TiO_2 with dual active sites for selective photocatalytic CO_2 reduction (Small 2/2018). *Small* **2018**, *14*, 1870008.

[54] Yazdanpanah, M.; Fereidooni, M.; Márquez, V.; Paz, C. V.; Saelee, T.; Villanueva, M. S.; Rittiruam, M.; Khajondetchairit, P.; Praserthdam, S.; Praserthdam, P. The underlying catalytic role of oxygen vacancies in fatty acid methyl esters ketonization over TiO_x catalysts. *ChemSusChem* **2024**, *17*, e202301033.

[55] Zhao, J.; Li, Y. X.; Zhu, Y. Q.; Wang, Y.; Wang, C. Y. Enhanced CO_2 photoreduction activity of black TiO_2-coated Cu nanoparticles under visible light irradiation: Role of metallic Cu. *Appl. Catal. A: Gen.* **2016**, *510*, 34–41.

[56] Fu, F. Y.; Shown, I.; Li, C. S.; Raghunath, P.; Lin, T. Y.; Billo, T.; Wu, H. L.; Wu, C. I.; Chung, P. W.; Lin, M. C. et al. KSCN-induced interfacial dipole in black TiO_2 for enhanced photocatalytic CO_2 reduction. *ACS Appl. Mater. Interfaces* **2019**, *11*, 25186–25194.

[57] Han, L. J.; Su, B. T.; Liu, G.; Ma, Z.; An, X. C. Synthesis of oxygen vacancy-rich black TiO_2 nanoparticles and the visible light photocatalytic performance. *Mol. Catal.* **2018**, *456*, 96–101.

[58] Lin, Z.; Lee, G. H.; Liu, C. M.; Lee, I. S. Controls in wettability of TiO_x films for biomedical applications. *Surf. Coat. Technol.* **2010**, *205*, S391–S397.

[59] Zimbone, M.; Cacciato, G.; Sanz, R.; Carles, R.; Gulino, A.; Privitera, V.; Grimaldi, M. G. Black TiO_x photocatalyst obtained by laser irradiation in water. *Catal. Commun.* **2016**, *84*, 11–15.

[60] Zimbone, M.; Cacciato, G.; Boutinguiza, M.; Gulino, A.; Cantarella, M.; Privitera, V.; Grimaldi, M. G. Hydrogenated black-TiO_x: A facile and scalable synthesis for environmental water purification. *Catal. Today* **2019**, *321–322*, 146–157.

[61] Schulze, P. D.; Shaffer, S. L.; Hance, R. L.; Utley, D. L. Adsorption of water on rhenium studied by XPS. *J. Vac. Sci. Technol. A* **1983**, *1*, 97–99.

[62] Ye, R. P.; Ding, J.; Gong, W. B.; Argyle, M. D.; Zhong, Q.; Wang, Y. J.; Russell, C. K.; Xu, Z. H.; Russell, A. G.; Li, Q. H. et al. CO_2 hydrogenation to high-value products via heterogeneous catalysis. *Nat. Commun.* **2019**, *10*, 5698.

[63] Shu, Y. J.; Ji, J.; Zhou, M.; Liang, S. M.; Xie, Q.; Li, S. T.; Liu, B. Y.; Deng, J. G.; Cao, J. P.; Liu, S. W. et al. Selective photocatalytic oxidation of gaseous ammonia at ppb level over Pt and F modified TiO_2. *Appl. Catal. B: Environ.* **2022**, *300*, 120688.

[64] Cao, L.; Chen, L.; Wu, X. D.; Ran, R.; Xu, T. F.; Chen, Z.; Weng, D. TRA and DRIFTS studies of the fast SCR reaction over CeO_2/TiO_2 catalyst at low temperatures. *Appl. Catal. A: Gen.* **2018**, *557*, 46–54.

[65] Fan, J.; Ning, P.; Song, Z. X.; Liu, X.; Wang, L. Y.; Wang, J.; Wang, H. M.; Long, K. X.; Zhang, Q. L. Mechanistic aspects of NH_3-SCR reaction over CeO_2/TiO_2-ZrO_2-SO_4^{2-} catalyst: *In situ* DRIFTS investigation. *Chem. Eng. J.* **2018**, *334*, 855–863.

[66] Feng, X.; Han, Z. T.; Li, C. L.; Liu, T. J. Investigation of the promotional effect of W modification on selective catalytic reduction performance of $Ce_{0.4}ZrO_x$ catalysts. *Energy Fuels* **2024**, *38*, 6269–6280.

[67] Liu, Z. M.; Zhang, S. X.; Li, J. H.; Ma, L. L. Promoting effect of MoO_3 on the NO_x reduction by NH_3 over CeO_2/TiO_2 catalyst studied with *in situ* DRIFTS. *Appl. Catal. B: Environ.* **2014**, *144*, 90–95.

[68] Zhu, F.; Wang, Z. Q.; Huang, J. C.; Hu, W.; Xie, D.; Qiao, Y. Efficient adsorption of ammonia on activated carbon from hydrochar of pomelo peel at room temperature: Role of chemical components in feedstock. *J. Clean. Prod.* **2023**, *406*, 137076.

[69] Barzetti, T.; Selli, E.; Moscotti, D.; Forni, L. Pyridine and ammonia as probes for FTIR analysis of solid acid catalysts. *J. Chem. Soc., Faraday Trans.* **1996**, *92*, 1401–1407.

[70] Chen, L.; Si, Z. C.; Wu, X. D.; Weng, D. DRIFT study of CuO–CeO_2–TiO_2 mixed oxides for NO_x reduction with NH_3 at low temperatures. *ACS Appl. Mater. Interfaces* **2014**, *6*, 8134–8145.

[71] Michalow-Mauke, K. A.; Lu, Y.; Kowalski, K.; Graule, T.; Nachtegaal, M.; Kröcher, O.; Ferri, D. Flame-made WO_3/CeO_x-TiO_2 catalysts for selective catalytic reduction of NO_x by NH_3. *ACS Catal.* **2015**, *5*, 5657–5672.

[72] Tuntithavornwat, S.; Saisawang, C.; Ratvijitvech, T.; Watthanaphanit, A.; Hunsom, M.; Kannan, A. M. Recent development of black TiO_2 nanoparticles for photocatalytic H_2 production: An extensive review. *Int. J. Hydrogen Energy* **2024**, *55*, 1559–1593.

[73] Ouslimane, T.; Et-Taya, L.; Elmaimouni, L.; Benami, A. Impact of absorber layer thickness, defect density, and operating temperature on the performance of $MAPbI_3$ solar cells based on ZnO electron transporting material. *Heliyon* **2021**, *7*, e06379.

[74] Balog, Á.; Samu, G. F.; Pető, S.; Janáky, C. The mystery of black TiO_2: Insights from combined surface science and *in situ* electrochemical methods. *ACS Mater. Au* **2021**, *1*, 157–168.

[75] Saidi, F.; Mahmoudi, A.; Laidi, K.; Hidouri, T.; Nasr, S. Structural, electronic and optical properties of M-doped anatase TiO_2 (M = Fe or Au): A first principle investigation. *Comput. Condens. Matter* **2021**, *28*, e00576.

[76] Thaines, E. H. N. S.; Oliveira, A. C.; Pocrifka, L. A.; Duarte, H. A.; Freitas, R. G. Influence of Fe-doping on the structural and electronic properties of the TiO_2 anatase: Rutile. *J. Phys. Chem. C* **2023**, *127*, 22518–22529.

[77] Zhang, C. C.; Wang, L. T.; Etim, U. J.; Song, Y. B.; Gazit, O. M.; Zhong, Z. Y. Oxygen vacancies in Cu/TiO_2 boost strong metal-support interaction and CO_2 hydrogenation to methanol. *J. Catal.* **2022**, *413*, 284–296.

[78] Li, Q.; Wang, C. Q.; Wang, H. L.; Chen, J.; Chen, J.; Jia, H. P. Disclosing support-size-dependent effect on ambient light-driven photothermal CO_2 hydrogenation over nickel/titanium dioxide. *Angew. Chem., Int. Ed.* **2024**, *63*, e202318166.

[79] Ghampson, I. T.; Pecchi, G.; Fierro, J. L. G.; Videla, A.; Escalona, N. Catalytic hydrodeoxygenation of anisole over $Re\text{-}MoO_x/TiO_2$ and $Re\text{-}VO_x/TiO_2$ catalysts. *Appl. Catal. B: Environ.* **2017**, *208*, 60–74.

[80] Zhao, H. B.; Yu, R. F.; Ma, S. C.; Xu, K. Z.; Chen, Y.; Jiang, K.; Fang, Y.; Zhu, C. X.; Liu, X. C.; Tang, Y. et al. The role of Cu_1-O_3 species in single-atom Cu/ZrO_2 catalyst for CO_2 hydrogenation. *Nat. Catal.* **2022**, *5*, 818–831.

[81] Wang, Y. H.; Liu, Y.; Tan, L.; Lin, X. H.; Fang, Y. X.; Lu, X. F.; Hou, Y. D.; Zhang, G. G.; Wang, S. B. Confining ultrafine Pt nanoparticles on In_2O_3 nanotubes for enhanced selective methanol production by CO_2 hydrogenation. *J. Mater. Chem. A* **2023**, *11*, 26804–26811.

[82] Cárdenas-Arenas, A.; Quindimil, A.; Davó-Quiñonero, A.; Bailón-García, E.; Lozano-Castelló, D.; De-La-Torre, U.; Pereda-Ayo, B.; González-Marcos, J. A.; González-Velasco, J. R.; Bueno-López, A. Isotopic and *in situ* DRIFTS study of the CO_2 methanation mechanism using Ni/CeO_2 and Ni/Al_2O_3 catalysts. *Appl. Catal. B: Environ.* **2020**, *265*, 118538.

[83] Phongprueksathat, N.; Ting, K. W.; Mine, S.; Jing, Y.; Toyoshima, R.; Kondoh, H.; Shimizu, K. I.; Toyao, T.; Urakawa, A. Bifunctionality of Re supported on TiO_2 in driving methanol formation in low-temperature CO_2 hydrogenation. *ACS Catal.* **2023**, *13*, 10734–10750.

[84] Pérez-Hernández, R.; Martínez, A. G.; Galicia, G. M.; García, M. E. F.; Nuñez, O. C.; Hernández, M. V.; López, P.; Wing, C. E. G. Carbon cycle using the CO_2 conversion to methane as environmental feasibility on Ni/TiO_2–Na nanotubes catalysts. *Renew. Energy* **2023**, *217*, 119145.

[85] Zhang, D.; Li, B. H.; Li, Y. L.; Zhao, J.; Wang, X. J.; Li, F. T. Efficient photocatalytic CO_2 methanation via promoted conversion of bridge *CO over surface K^+ on ultrathin TiO_2. *Mol. Catal.* **2023**, *549*, 113467.

[86] Vrijburg, W. L.; Moioli, E.; Chen, W.; Zhang, M.; Terlingen, B. J. P.; Zijlstra, B.; Filot, I. A. W.; Züttel, A.; Pidko, E. A.; Hensen, E. J. M. Efficient base-metal $NiMn/TiO_2$ catalyst for CO_2 methanation. *ACS Catal.* **2019**, *9*, 7823–7839.

[87] Zhou, Z.; Li, J. J.; You, Z. X. A facile TiO_2 containing oxygen vacancies and hydroxyl as a Ru-loaded underlay for CO_2 hydrogenation to CH_4. *Appl. Surf. Sci.* **2022**, *587*, 152856.

[88] Zhang, Z. H.; Zhang, L. Y.; Yao, S. Y.; Song, X. Z.; Huang, W. X.; Hülsey, M. J.; Yan, N. Support-dependent rate-determining step of CO_2 hydrogenation to formic acid on metal oxide supported Pd catalysts. *J. Catal.* **2019**, *376*, 57–67.

[89] Wang, C. F.; Lu, Y. L.; Zhang, Y.; Fu, H.; Sun, S. Z.; Li, F.; Duan, Z. Y.; Liu, Z.; Wu, C. F.; Wang, Y. H. et al. Ru-based catalysts for efficient CO_2 methanation: Synergistic catalysis between oxygen

vacancies and basic sites. *Nano Res.* **2023**, *16*, 12153–12164.

[90] Cui, W. G.; Zhuang, X. Y.; Li, Y. T.; Zhang, H. B.; Dai, J. J.; Zhou, L.; Hu, Z. P.; Hu, T. L. Engineering Co/MnO heterointerface inside porous graphitic carbon for boosting the low-temperature CO_2 methanation. *Appl. Catal. B: Environ.* **2021**, *287*, 119959.

[91] Zhao, Z. Y.; Jiang, Q. R.; Wang, Q. X.; Wang, M. Z.; Zuo, J. C.; Chen, H. M.; Kuang, Q.; Xie, Z. X. Effect of rutile content on the catalytic performance of Ru/TiO_2 catalyst for low-temperature CO_2 methanation. *ACS Sustainable Chem. Eng.* **2021**, *9*, 14288–14296.

[92] Raskó, J.; Kiss, J. Surface species and gas phase products in the preferential oxidation of CO on TiO_2-supported Au-Rh bimetallic catalysts. *React. Kinet. Catal. Lett.* **2007**, *90*, 389–399.

[93] Han, C. Q.; Zhang, R. M.; Ye, Y. H.; Wang, L.; Ma, Z. Y.; Su, F. Y.; Xie, H. Q.; Zhou, Y.; Wong, P. K.; Ye, L. Q. Chainmail co-catalyst of NiO shell-encapsulated Ni for improving photocatalytic CO_2 reduction over g-C_3N_4. *J. Mater. Chem. A* **2019**, *7*, 9726–9735.

[94] Ting, K. W.; Toyao, T.; Siddiki, S. M. A. H.; Shimizu, K. I. Low-temperature hydrogenation of CO_2 to methanol over heterogeneous TiO_2-supported Re catalysts. *ACS Catal.* **2019**, *9*, 3685–3693.

[95] Yang, B.; Wang, Y. F.; Gao, B.; Zhang, L. X.; Guo, L. M. Size-dependent active site and its catalytic mechanism for CO_2 hydrogenation reactivity and selectivity over Re/TiO_2. *ACS Catal.* **2023**, *13*, 10364–10374.

[96] Shi, X. Y.; Zhang, C. B.; He, H.; Shou, M.; Tanaka, K. I.; Sugihara, S.; Ando, Y. Activation of Pt/TiO_2 catalysts by structural transformation of Pt-sites. *Catal. Lett.* **2006**, *107*, 1–4.

[97] Wang, K.; Jiang, R. M.; Peng, T.; Chen, X.; Dai, W. X.; Fu, X. Z. Modeling the effect of Cu doped TiO_2 with carbon dots on CO_2 methanation by H_2O in a photo-thermal system. *Appl. Catal. B: Environ.* **2019**, *256*, 117780.

[98] Zhang, H. N.; Li, Y. F.; Wang, J. Z.; Wu, N. N.; Sheng, H.; Chen, C. C.; Zhao, J. C. An unprecedent hydride transfer pathway for selective photocatalytic reduction of CO_2 to formic acid on TiO_2. *Appl. Catal. B: Environ.* **2021**, *284*, 119692.

[99] Zhang, Z. L.; Kladi, A.; Verykios, X. E. Surface species formed during CO and CO_2 hydrogenation over Rh/TiO_2 (W^{6+}) catalysts investigated by FTIR and mass-spectroscopy. *J. Catal.* **1995**, *156*, 37–50.

[100] Han, B.; Guo, Y. L.; Huang, Y. K.; Xi, W.; Xu, J.; Luo, J.; Qi, H. F.; Ren, Y. J.; Liu, X. Y.; Qiao, B. T. et al. Strong metal-support interactions between Pt single atoms and TiO_2. *Angew. Chem. Int. Ed.* **2020**, *59*, 11824–11829.